Check for updates

Chemical Biology & Drug Design

WILEY

RESEARCH ARTICLE

Design, Synthesis, and Anticancer Assessment of Benzylated Pyrrole-Based Pyrido[2,3-*d*]Pyrimidines as Thymidylate Synthase Inhibitors

Adarsh Kumar[1] | Sonu Rajput[2] | Ankit Kumar Singh[1,3] | Vineet Prajapati[1] | Amita Verma[3] | Prateek Pathak[4] | Umashanker Navik[2] | Jurica Novak[5] | Pradeep Kumar[1]

[1]Department of Pharmaceutical Sciences and Natural Products, Central University of Punjab, Bathinda, India | [2]Department of Pharmacology, Central University of Punjab, Bathinda, India | [3]Bioorganic and Medicinal Chemistry Research Laboratory, Department of Pharmaceutical Sciences, Sam Higginbottom University of Agriculture, Technology and Sciences, Prayagraj, India | [4]Department of Pharmaceutical Analysis, Quality Assurance and Pharmaceutical Chemistry, School of Pharmacy, GITAM (Deemed to be University), Hyderabad Campus, Hyderabad, India | [5]Center for Informatics and Computing, Ruđer Bošković Institute, Zagreb, Croatia

Correspondence: Jurica Novak (jnovak@irb.hr) | Pradeep Kumar (pradeepyadav27@gmail.com)

Received: 16 September 2025 | **Revised:** 19 December 2025 | **Accepted:** 29 December 2025

Keywords: anticancer | colorectal cancer | pyrido[2,3-d]pyrimidines | synthesis

ABSTRACT

Globally, colorectal cancer (CRC) is the second most common cause of cancer-related deaths and the third most common cancer. Thymidylate synthase (TS), a key enzyme involved in DNA biosynthesis, has emerged as a promising molecular target for anticancer therapy. In the present study, we designed and synthesized a series of 22 benzylated pyrrole-based pyrido[2,3-*d*]pyrimidines using Claisen Schmidt and Michael addition reactions, and evaluated their anticancer potential against four human cancer cell lines: HCT 116 (colorectal), A549 (lung), MCF-7 (breast), and MDA-MB-231 (triple-negative breast cancer) as well as for TS inhibitory potential. Compounds 1c and 2i exhibited potent TS inhibition with IC_{50} values of 11.50 ± 1.08 nM and 17.12 ± 0.91 nM, respectively, comparable to the standard drug raltitrexed (IC_{50} = 12.51 ± 0.91 nM). Molecular docking studies revealed stronger binding affinities of these compounds compared to raltitrexed, involving key interactions with the catalytic residue Cys195 of TS. Additionally, compounds 1c and 2i exhibited good stability in 300 ns molecular dynamics simulations along with acceptable drug-like properties and oral bioavailability. These findings suggest that compounds 1c and 2i are promising lead candidates for the development of TS inhibitors.

1 | Introduction

Cancer ranks second in terms of cause of deaths after cardiovascular diseases, despite the availability of many chemotherapeutic treatments (Deep et al. 2016; Narella et al. 2019). Among all reported cancers, colorectal cancer (CRC) is the second most common cause of cancer-related death and the third most common cancer across the globe (Kumar et al. 2022). Colorectal cancer accounted for 1,926,118 (9.6%) of the 19,964,811 new cases of cancer that were reported worldwide in 2022, and 904,000 of these cases resulted in death, according to the Globocan report. This is equivalent to almost 1 in 10 cases and deaths from cancer (Sung et al. 2021). Genetic predisposition, socioeconomic status, environmental exposures, dietary habits, other lifestyle factors,

Abbreviations: Aq., aqueous; CRC, colorectal cancer; dTMP, deoxythymidine monophosphate; dUMP, deoxyuridine monophosphate; Eq., equivalent; GC–MS, gas chromatography–mass spectrometry; hTS, human thymidylate synthase; IC_{50}, concentration which inhibits 50% of the tested population; nM, nano molar; RAL, raltitrexed; THF, tetrahydrofolate; TS, thymidylate synthase; μM, micro molar.

© 2026 John Wiley & Sons Ltd.

and/or screening techniques are a few of the potential contributing factors to these differences (Arnold et al. 2017; Fitzmaurice et al. 2018; Raj et al. 2023).

Because thymidylate synthase (TS) is important for DNA biosynthesis, it has gained attention in cancer chemotherapy. TS is the rate-limiting enzyme in the *de novo* synthesis of 2′-de oxythymidine-5′-monophosphate. TS catalyzes the reducing methylation of dUMP into dTMP by using methylene tetrahydrofolate to be the source of one carbon methyl group. TS inhibitors referred to as folate binding site inhibitors and dUMP (pyrimidine) binding site inhibitors link to the active site and imitate the cofactor mTHF or the substrate dUMP, respectively. Capcitabine as well as 5-fluorouracil are examples of dUMP binding inhibiting agents, while pemetrexed, raltitrexed, pralatrexate, as well as nolatrexed are examples of folate binding site inhibitors (Kumar et al. 2022; Shih et al. 1997; Ward et al. 1992). The main drawbacks of this treatment are the drugs' cytotoxicity along with the development of chemoresistance, which can be brought on by a number of things but is usually connected to the overexpression or dysregulation of TS. Therefore, developing molecules that maintain the inactive conformation of hTS may help to alleviate this problem (Garg et al. 2010; Gonen and Assaraf 2012; Taddia et al. 2015).

Nitrogen-containing heterocyclic compounds are known pharmacophores with a variety of pharmacological actions. These compounds include pyrrolo-benzodiazepines, pyrido[2,3-*d*] pyrimidines, isatin, β-lactam, quinoxaline, pyrazole, carbazole, imidazole, triazole, indole, pyrimidine, quinazoline, benzimidazole, quinoline, and pyridine. Less research has been done on the impact of pyrido[2,3-*d*]pyrimidines on cancer compared to the remaining nitrogen-containing heterocyclic derivatives mentioned above (Kumar, Singh, et al. 2023).

We conducted a thorough literature search to investigate the potential use of pyrido[2,3-d]pyridine in the treatment/management of cancer. We observed that various cancer targets have been reported globally, including tyrosine kinase, ABL kinase, phosphatidylinositol-3kinase, dihydrofolate reductase, cyclin-dependent kinase, phosphodiesterase, p38 mitogen-activated protein kinases, KRAS, BCR-ABL, and fibroblast growth factor receptors (Kumar, Bhagat, et al. 2023). In keeping with our earlier research, focused on pharmacophore mapping, binding free energy calculations, and virtual screening of pyrido[2,3-*d*]pyrimidine ligands to identify the pharmacophoric properties of pyrido[2,3-*d*] pyrimidines as TS inhibitors (Kumar, Novak, et al. 2023), this study is a continuation of our previous study which has revealed that pyrrole/alkylated pyrrole-based compound with chloro at para-position of aromatic ring had an IC_{50} of 15 nM against TS with promising anticancer activity (Kumar et al. 2025). Therefore, based on SAR studies, we have synthesized benzylated pyrrole-based pyrido[2,3-d]pyrimidine/alkylated pyrido[2,3-*d*]pyrimidines and found that compound 1c with methoxy at the meta position has an IC_{50} of 11.50 nM against TS which is lower than raltitrexed and previously reported compounds.

2 | Material and Methods

2.1 | General Chemistry

For column chromatography, silica gel with a mesh size of 60–120 was utilized. Using TMS (=0) as an internal standard, the ^{1}H and ^{13}C NMR spectra in $CDCl_3/d_6$-DMSO were recorded using a 600 MHz Jeol NMR spectrometer. Chemical shifts (d) are expressed in parts per million (ppm), coupling constants (J) are expressed in Hertz (Hz), and splitting patterns are denoted by the characters singlet (s), doublet (d), triplet (t), as well as multiplet (m). Uncorrected melting points were determined using a Stuart melting point instrument (SMP-30) and an open glass capillary tube. At 70 eV, SHIMADZU GC–MS recorded GC–MS spectra. The Spectroline Fluorescence Analysis Cabinet (Model CM-10A) was used to visualize TLC under the UV light. The Triple TOF 5600 (Make-SCIEX) was used to record the HRMS spectra of representative inhibitors. With a particle size of 5 μm, HPLC of potent derivatives, 1c and 2i was carried out using an Agilent 1260 Infinity II using a column Eclipse XDB-C18.

2.2 | Synthetic Process and Spectral Data

2.2.1 | General Protocol for Synthesis of Intermediate (I)

In a round bottom flask, potassium hydroxide (5 Eq.) in acetonitrile (25 mL) was stirred for 15–20 min. 1*H*-pyrrole-2-carbaldehyde (1 Eq.) was added to it and the reaction mixture was stirred for 20–30 min. Then, benzyl bromide (1.25 Eq.) was added to the stirred mixture. The reaction was monitored by TLC (08% ethylacetate in pet ether). After the completion of reaction (≈5 h), workup was done using ethyl acetate and water. Then the product was concentrated on rotary evaporator (Kumar et al. 2024).

2.2.2 | 1-Benzyl-1*H*-Pyrrole-2-Carbaldehyde

Yield: 93%; **^{1}H NMR** (600 MHz, $CDCl_3$) δ 9.55 (s, 1H), 7.30–7.27 (m, 2H), 7.26–7.24 (m, 1H), 7.13 (d, J = 7.3 Hz, 2H), 6.96 (d, J = 3.5 Hz, 2H), 6.27–6.24 (m, 1H), 5.55 (s, 2H); **^{13}C NMR** (151 MHz, $CDCl_3$) δ 179.61, 137.66, 131.50, 128.90, 128.80, 127.82, 127.38, 124.92, 110.24, 52.04. GC–MS (EI) calculated for $C_{12}H_{11}NO$, 185.22 $[M]^+$; observed: 184.22.

2.2.3 | General Procedure for the Synthesis of Intermediate (II)

To dissolve cyanoacetic ester (10 g, 1 Eq.), 6.011 g of sodium ethoxide (1 Eq.) was added to 100 mL of pure methanol in a round bottom flask. After that, the mixture was heated over reflux for 10 h while 5.305 g of urea (1 eq) was added. The product was then separated from the alcohol and dissolved in water. The 6-amino pyrimidine-2,4(1H,3H)-dione precipitated out when acetic acid was added, and it was filtered out (Barrowcliff and Carr 1921).

17470285, 2026, 1, Downloaded from https://onlinelibrary.wiley.com/doi/10.1111/cbdd.70240 by University Of Notre Dame, Wiley Online Library on [29/10/2026]. See the Terms and Conditions (https://onlinelibrary.wiley.com/terms-and-conditions) on Wiley Online Library for rules of use; OA articles are governed by the applicable Creative Commons License

2.2.4 | General Procedure for the Synthesis of Substituted Chalcone (III)

1-Benzyl-1*H*-pyrrole-2-carbaldehyde (I) (1 Eq.) was added into methanol then agitated for 12 min in a 100 mL round bottom flask (RBF). 20% Aq. solution of sodium hydroxide was added to the reaction mixture. Added one equivalent of substituted acetophenone to the reaction mixture after 15 min, and stirred for 2–8 h. TLC (20% ethylacetate in pet ether) was used to track the reaction's progress. On completion of the reaction, the reaction mixture was filtered, cleaned, and crystallized in methanol. The product was then further purified using column chromatography (7% ethylacetate in pet ether) (Kumar, Kumar, et al. 2023).

2.2.5 | General Procedure for the Synthesis of Benzylated Pyrrole-Based Pyrido[2,3-d]Pyrimidines (1a–1k)

Substituted chalcone (1 Eq.) was immersed in methanol and swirled for 15 min in a 100 mL round bottom flask. A 40% Aq. solution of sodium hydroxide was added to the reaction mixture. The reaction mixture was refluxed for 14–20 h after the addition of the already synthesized intermediate I (1 Eq.) after 15 min. The TLC (20% Ethyl acetate & petroleum ether) was used to track the reaction's progress. The reaction mixture was passed through filters, cleaned, as well as recrystallized in methanol once the reaction was finished. The produced compounds were then further purified using column chromatography (7% ethyl acetate & petroleum ether) (Kuday et al. 2014) (Supporting Information).

2.2.6 | 5-(1-Benzyl-1*H*-Pyrrol-2-Yl)-7-(4-Bromophenyl) pyrido[2,3-d]Pyrimidine -2,4(1*H*,3*H*)-Dione (1a)

Yield: 49%; yellow powder; **mp:** 152–154°C; **^{1}H NMR** (600 MHz, DMSO-d6) δ (ppm): 11.65 (s, 1H), 11.26 (s, 1H), 8.00 (d, J = 8.7 Hz, 2H), 7.71 (d, J = 8.6 Hz, 2H), 7.39 (s, 1H), 7.15 (d, J = 7.9 Hz, 2H), 7.12 (d, J = 7.4 Hz, 1H), 6.94–6.93 (m, 1H), 6.88 (d, J = 6.5 Hz, 2H), 6.21 (dd, J = 3.6, 1.8 Hz, 1H), 6.15 (d, J = 3.6 Hz, 1H), 4.94 (s, 2H); **^{13}C NMR** (151 MHz, DMSO-d6) δ (ppm): 161.81, 158.00, 154.02, 150.74, 145.06, 139.29, 136.41, 132.36, 130.87, 129.79, 128.68, 127.48, 127.47, 124.85, 124.21, 119.30, 116.17, 110.69, 108.32, 51.11; **GC–MS** (EI) calculated for $C_{24}H_{17}BrN_4O_2$, 472.05 $[M]^+$; observed: [M + H]; 473; **HRMS** (TOF MS) calculated for $C_{24}H_{17}BrN_4O_2$, 473.0613 [M + H]; observed [M + H]: 473.0629.

2.2.7 | 5-(1-Benzyl-1*H*-Pyrrol-2-Yl)-7-(4-Methoxyphenyl) pyrido[2,3-d]Pyrimidine -2,4(1*H*,3*H*)-Dione (1b)

Yield: 51%; yellowish powder; **mp**: 150–152°C; **^{1}H NMR** (600 MHz, DMSO-d6) δ (ppm): 11.56 (s, 1H), 11.18 (s, 1H), 8.14 (d, J = 8.1 Hz, 1H), 8.03 (d, J = 8.9 Hz, 2H), 7.31 (s, 1H), 7.16 (t, J = 6.4 Hz, 2H), 7.03 (d, J = 7.3 Hz, 2H), 6.90 (t, J = 7.2 Hz, 3H), 6.1 6 (d, J = 4.3 Hz, 2H), 4.93 (s, 2H), 3.83 (s, 3H); **^{13}C NMR** (151 MHz, DMSO-d6) δ (ppm): 163.05, 159.66, 158.52, 158.34, 153.19, 152.82, 150.13, 144.34, 138.37, 129.89, 128.12, 126.93, 123.53, 119.56, 118.14, 115.98, 112.62, 110.02, 59.74, 55.26; **GC–MS** (EI) calculated for $C_{25}H_{20}N_4O_3$, 424.46 $[M]^+$; observed: 424.10.

2.2.8 | 5-(1-Benzyl-1*H*-Pyrrol-2-Yl)-7-(3-Methoxyphenyl) pyrido[2,3-d]Pyrimidine -2,4(1*H*,3*H*)-Dione (1c)

Yield: 50%; yellowish powder; **% Purity** ≥ 98 (HPLC); **mp**: 150–152°C; **^{1}H NMR** (600 MHz, DMSO-d6) δ (ppm): 11.51 (s, 1H), 11.25 (s, 1H), 8.32 (s, 1H), 7.74–7.70 (m, 2H), 7.67 (s, 1H), 7.60 (d, J = 6.6 Hz, 1H), 7.45 (t, J = 7.8 Hz, 1H), 7.41 (t, J = 7.8 Hz, 1H), 7.16 (t, J = 7.4 Hz, 1H), 7.13–7.03 (m, 3H), 6.95–6.87 (m, 2H), 4.35 (s, 2H), 3.85 (s, 3H); **^{13}C NMR** (151 MHz, DMSO-d6) δ (ppm): 163.59, 160.20, 159.06, 158.87, 153.72, 153.36, 150.67, 144.87, 138.90, 130.42, 128.66, 127.47, 124.08, 124.07, 120.09, 119.53, 118.67, 116.52, 113.01, 110.56, 108.28, 60.27, 55.80; **GC–MS** (EI) calculated for $C_{25}H_{20}N_4O_3$, 424.46 $[M]^+$; observed: 424.10.

2.2.9 | 5-(1-Benzyl-1*H*-Pyrrol-2-Yl)-7-(4-Chlorophenyl) pyrido[2,3-d]Pyrimidine -2,4(1*H*,3*H*)-Dione (1d)

Yield: 47%; yellow powder; **mp**: 156–158°C; **^{1}H NMR** (600 MHz, DMSO-d6) δ (ppm): 11.66 (s, 1H), 11.27 (s, 1H), 8.18 (d, J = 8.3 Hz, 1H), 8.07 (d, J = 8.2 Hz, 2H), 7.62 (d, J = 8.3 Hz, 1H), 7.57 (d, J = 8.1 Hz, 2H), 7.39 (s, 1H), 7.18–7.15 (m, 2H), 7.12 (d, J = 7.3 Hz, 1H), 6.94–6.88 (m, 3H), 4.95 (s, 2H); **^{13}C NMR** (151 MHz, DMSO-d6) δ (ppm): 162.68, 161.83, 159.69, 157.94, 154.02, 150.77, 145.07, 139.29, 135.95, 130.89, 129.56, 129.43, 128.68, 127.48, 124.21, 119.35, 110.70, 108.33, 107.58, 51.13; **GC–MS** (EI) calculated for $C_{24}H_{17}ClN_4O_2$, 428.87 $[M]^+$; observed: 427.90.

2.2.10 | 5-(1-Benzyl-1*H*-Pyrrol-2-Yl)-7-(*p*-Tolyl) pyrido[2,3-d]Pyrimidine -2,4(1*H*,3*H*)-Dione (1e)

Yield: 56%; light yellow powder; **mp**: 150–152°C; **^{1}H NMR** (600 MHz, DMSO-d6) δ (ppm): 11.59 (s, 1H), 11.22 (s, 1H), 7.94 (d, J = 8.2 Hz, 2H), 7.32 (s, 1H), 7.30 (d, J = 8.0 Hz, 2H), 7.16 (t, J = 7.3 Hz, 2H), 7.11 (t, J = 7.3 Hz, 1H), 6.95–6.91 (m, 1H), 6.88 (d, J = 7.4 Hz, 2H), 6.20 (dd, J = 3.6, 1.8 Hz, 1H), 6.17–6.13 (m, 1H), 4.94 (s, 2H), 2.37 (s, 3H); **^{13}C NMR** (151 MHz, DMSO-d6) δ (ppm): 161.88, 159.30, 153.98, 150.78, 144.74, 140.97, 139.32, 134.49, 131.03, 129.98, 128.68, 127.73, 127.54, 127.43, 124.05, 119.05, 110.50, 108.27, 107.05, 51.09, 21.46; **GC–MS** (EI) calculated for $C_{25}H_{20}N_4O_2$, 408.46 $[M]^+$; observed: 409.

2.2.11 | 5-(1-Benzyl-1*H*-Pyrrol-2-Yl)-7-(2,4-Dibromophenyl)pyrido[2,3-d] Pyrimidine -2,4(1*H*,3*H*)-Dione (1f)

Yield: 44%; brown powder; **mp**: 160–162°C; **^{1}H NMR** (600 MHz, DMSO-d6) δ (ppm): 11.65 (s, 1H), 11.26 (s, 1H), 8.00 (d, J = 8.6 Hz, 2H), 7.39 (s, 1H), 7.17 (s, 1H), 7.15 (d, J = 7.8 Hz, 2H), 7.04 (d, J = 6.9 Hz, 1H), 6.95–6.92 (m, 1H), 6.88 (d, J = 6.6 Hz, 2H), 6.22 (dd, J = 3.6, 1.8 Hz, 1H), 6.16–6.14 (m, 1H), 4.94 (s, 2H); **^{13}C NMR** (151 MHz, DMSO-d6) δ (ppm): 167.20, 161.81, 150.76, 150.74, 132.36, 132.18, 132.17, 131.82, 131.81, 130.87, 129.80, 129.78, 128.69, 128.68, 127.48, 127.47, 127.24, 127.23,

17470285, 2026, 1, Downloaded from https://onlinelibrary.wiley.com/doi/10.1111/cbdd.70240 by University Of Notre Dame, Wiley Online Library on [29/10/2026]. See the Terms and Conditions (https://onlinelibrary.wiley.com/terms-and-conditions) on Wiley Online Library for rules of use; OA articles are governed by the applicable Creative Commons License

127.17, 127.15, 124.21, 108.32, 51.12; **GC–MS** (EI) calculated for $C_{24}H_{16}Br_2N_4O_2$, 552.22 $[M]^+$; observed: 522.30.

2.2.12 | 5-(1-Benzyl-1*H*-Pyrrol-2-Yl)-7-(4-Fluorophenyl) Pyrido[2,3-d]Pyrimidine -2,4(1*H*,3*H*)-Dione (1g)

Yield: 52%; yellow powder; **mp**: 160–162°C; **^{1}H NMR** (600 MHz, DMSO-d6) δ (ppm): 11.63 (s, 1H), 11.24 (s, 1H), 8.11 (dd, J = 8.8, 5.6 Hz, 2H), 7.37 (s, 1H), 7.34 (t, J = 8.8 Hz, 2H), 7.16 (d, J = 7.8 Hz, 2H), 7.12 (d, J = 7.4 Hz, 1H), 6.95–6.92 (m, 1H), 6.89 (d, J = 7.4 Hz, 2H), 6.21 (dd, J = 3.6, 1.8 Hz, 1H), 6.16–6.14 (m, 1H), 4.94 (s, 2H); **^{13}C NMR** (151 MHz, DMSO-d6) δ (ppm): 161.84, 158.16, 153.97, 150.77, 144.97, 139.30, 130.92, 130.22, 130.16, 128.68, 127.55, 127.47, 124.14, 119.17, 116.40, 116.25, 110.63, 108.30, 107.26, 51.11; **GC–MS** (EI) calculated for $C_{24}H_{17}FN_4O_2$, 412.42 $[M]^+$; observed: 411.95.

2.2.13 | 5-(1-Benzyl-1*H*-Pyrrol-2-Yl)-7-(3-Bromophenyl) Pyrido[2,3-d]Pyrimidine -2,4(1*H*,3*H*)-Dione (1h)

Yield: 48%; yellow powder; **mp**: 152–154°C; **^{1}H NMR** (600 MHz, DMSO-d6) δ (ppm): 11.66 (s, 1H), 11.29 (s, 1H), 8.27 (s, 1H), 8.15 (d, J = 7.2 Hz, 1H), 8.03 (d, J = 7.7 Hz, 1H), 7.71 (d, J = 17.3 Hz, 2H), 7.43 (d, J = 4.1 Hz, 1H), 7.16–7.14 (m, 1H), 7.11 (d, J = 6.1 Hz, 1H), 6.93 (s, 1H), 6.88 (d, J = 7.6 Hz, 2H), 6.25–6.21 (m, 1H), 6.19–6.13 (m, 1H), 4.93 (s, 2H); **^{13}C NMR** (151 MHz, DMSO-d6) δ (ppm): 163.51, 161.80, 157.37, 153.76, 150.72, 145.14, 139.48, 133.63, 131.52, 130.80, 130.34, 128.67, 127.47, 126.73, 124.25, 122.90, 119.55, 118.73, 110.81, 108.33, 107.85, 51.11; **GC–MS** (EI) calculated for $C_{24}H_{17}BrN_4O_2$, 472.05 $[M]^+$; observed: 472.

2.2.14 | 5-(1-Benzyl-1*H*-Pyrrol-2-Yl)-7-(2,4-Dichlorophenyl)Pyrido[2,3-d] Pyrimidine -2,4(1*H*,3*H*)-Dione (1i)

Yield: 42%; yellow powder; **mp**: 162–164°C; **^{1}H NMR** (600 MHz, DMSO-d6) δ (ppm): 11.65 (s, 1H), 11.25 (s, 1H), 8.07 (d, J = 8.7 Hz, 2H), 7.57 (d, J = 8.7 Hz, 2H), 7.39 (s, 1H), 7.04 (d, J = 8.2 Hz, 2H), 6.94 (s, 1H), 6.88 (d, J = 7.7 Hz, 2H), 6.22–6.20 (m, 1H), 6.15 (d, J = 3.2 Hz, 1H), 4.94 (s, 2H); **^{13}C NMR** (151 MHz, DMSO-d6) δ (ppm): 167.22, 161.82, 150.76, 150.74, 132.38, 132.36, 132.18, 132.17, 131.81, 130.87, 129.78, 128.69, 128.68, 127.48, 127.47, 127.23, 127.17, 127.15, 124.23, 124.21, 108.32, 51.12; **GC–MS** (EI) calculated for $C_{24}H_{16}Cl_2N_4O_2$, 463.31 $[M]^+$; observed: 463.20.

2.2.15 | 5-(1-Benzyl-1*H*-Pyrrol-2-Yl)-7-(2-Chlorophenyl) Pyrido[2,3-d]Pyrimidine -2,4(1*H*,3*H*)-Dione (1j)

Yield: 46%; yellow powder; **mp**: 156–158°C; **^{1}H NMR** (600 MHz, DMSO-d6) δ (ppm): 11.72 (s, 1H), 11.53 (s, 1H), 8.34 (d, J = 7.9 Hz, 2H), 7.26 (d, J = 3.1 Hz, 2H), 7.14 (d, J = 7.7 Hz, 3H), 7.05 (d, J = 3.3 Hz, 1H), 6.97 (s, 1H), 6.84 (d, J = 6.0 Hz, 2H), 6.14 (d, J = 12.1 Hz, 2H), 4.96 (s, 2H); **^{13}C NMR** (151 MHz, DMSO-d6) δ (ppm): 162.69, 161.38, 159.53, 152.77, 150.99, 138.22, 137.24, 131.97, 131.54, 131.42, 130.55, 128.67, 127.96, 127.33, 124.50, 123.78, 122.81, 120.20, 110.63, 109.45, 108.41, 51.14; **GC–MS** (EI) calculated for $C_{24}H_{17}ClN_4O_2$, 428.87 $[M]^+$; observed: 427.90.

2.2.16 | 5-(1-Benzyl-1*H*-Pyrrol-2-Yl)-7-(4-Nitrophenyl) Pyrido[2,3-d]Pyrimidine -2,4(1*H*,3*H*)-Dione (1k)

Yield: 54%; brown powder; **mp**: 164–166°C; **^{1}H NMR** (600 MHz, DMSO-d6) δ (ppm): 11.75 (s, 1H), 11.32 (s, 1H), 8.29 (d, J = 7.2 Hz, 2H), 8.26 (d, J = 8.9 Hz, 2H), 7.48 (s, 1H), 7.11 (t, J = 8.1 Hz, 2H), 7.06 (d, J = 8.4 Hz, 1H), 6.92 (d, J = 2.6 Hz, 1H), 6.84 (d, J = 7.5 Hz, 2H), 6.21 (d, J = 5.7 Hz, 1H), 6.12 (d, J = 3.3 Hz, 1H), 4.91 (s, 2H); **^{13}C NMR** (151 MHz, DMSO-d6) δ (ppm): 161.78, 156.62, 154.10, 150.74, 148.92, 145.31, 143.10, 139.29, 130.72, 129.01, 128.69, 127.49, 126.63, 124.49, 124.45, 120.38, 112.96, 110.91, 108.41, 51.13; **GC–MS** (EI) calculated for $C_{24}H_{17}N_5O_4$, 439.43 $[M]^+$; observed: 438.95.

2.2.17 | General Procedure for the Synthesis of Benzylated Pyrrole-Based Alkyl-Substituted Pyrido[2,3-d]Pyrimidine Derivatives 2(a–k)

For 10 to 15 min, potassium hydroxide (4 eq) within acetonitrile was stirred in a round bottom flask. After adding pyrido[2,3-*d*] pyrimidines 1(a-k) (1 Eq.) to the solution, the reaction mixture was agitated for 25–30 min at 0–4°C. The agitated mixture was then treated with 2.5 Eq. of methyl iodide. TLC (22.5% EA & pet ether) was used to track the reaction. Following the reaction's completion (2–6 h), ethyl acetate and water were used for workup, and column chromatography was used to purify the final product (12% EA & pet ether) (Kumar et al. 2024) (Supporting Information).

2.2.18 | 5-(1-Benzyl-1*H*-Pyrrol-2-Yl)-7-(4-Bromophenyl)-1,3-Dimethylpyrido[2,3-d] Pyrimidine -2,4(1*H*,3*H*)-Dione (2a)

Yield: 77%; yellow powder; **mp**: 154–156°C; **^{1}H NMR** (600 MHz, $CDCl_3$) δ (ppm): 7.87 (d, J = 8.6 Hz, 2H), 7.54 (d, J = 8.6 Hz, 2H), 7.35 (d, J = 4.9 Hz, 1H), 7.21 (d, J = 7.5 Hz, 2H), 6.91 (d, J = 7.0 Hz, 2H), 6.83 (d, J = 2.2 Hz, 1H), 6.83 (s, 1H), 6.28–6.25 (m, 2H), 4.96 (s, 2H), 3.09 (s, 3H), 2.60 (s, 3H); **^{13}C NMR** (151 MHz, $CDCl_3$) δ (ppm): 160.16, 158.00, 155.34, 146.03, 140.51, 137.49, 132.19, 131.70, 128.79, 128.62, 127.88, 127.28, 124.12, 123.72, 123.52, 119.51, 110.55, 110.08, 109.11, 51.26, 28.27, 26.83; **GC–MS** (EI) calculated for $C_{26}H_{21}BrN_4O_2$, 501.38 $[M]^+$; observed: [M + 1] 502.20.

2.2.19 | 5-(1-Benzyl-1*H*-Pyrrol-2-Yl)-7-(4-Methoxyphenyl)-1,3-Dimethylpyrido[2,3-d] Pyrimidine -2,4(1*H*,3*H*)-Dione (2b)

Yield: 78%; yellow powder; **mp**: 153–155°C; **^{1}H NMR** (600 MHz, $CDCl_3$) δ (ppm): 7.97 (d, J = 5.1 Hz, 2H), 7.33 (s, 1H), 7.19 (d, J = 7.9 Hz, 2H), 6.97 (d, J = 8.5 Hz, 2H), 6.85–6.83 (m, 1H), 6.82 (d, J = 5.8 Hz, 2H), 6.32 (t, J = 3.0 Hz, 1H), 6.27–6.23 (m, 2H), 4.96 (s, 2H), 3.87 (s, 3H), 3.42 (s, 3H), 3.11 (s, 3H); **^{13}C NMR** (151 MHz, $CDCl_3$) δ (ppm): 160.84, 159.15, 156.30, 151.74, 145.47, 140.38, 137.53, 131.71, 129.17, 127.84, 127.28, 123.83, 123.14, 118.99, 114.36, 113.96, 110.28, 109.02, 108.45, 55.55, 51.20, 30.16, 26.82. **GC–MS** (EI) calculated for $C_{27}H_{24}N_4O_3$, 452.51 $[M]^+$; observed: 552.35.

17470285, 2026, 1, Downloaded from https://onlinelibrary.wiley.com/doi/10.1111/cbdd.70240 by University Of Notre Dame, Wiley Online Library on [29/10/2026]. See the Terms and Conditions (https://onlinelibrary.wiley.com/terms-and-conditions) on Wiley Online Library for rules of use; OA articles are governed by the applicable Creative Commons License

2.2.20 | 5-(1-Benzyl-1*H*-Pyrrol-2-Yl)-7-(3-Methoxyphenyl)-1,3-Dimethylpyrido[2,3-d] Pyrimidine -2,4(1*H*,3*H*)-Dione (2c)

Yield: 78%; yellowish white powder; **mp**: 153–155°C; **^{1}H NMR** (600 MHz, $CDCl_3$) δ (ppm): **1H NMR** (600 MHz) δ (ppm): 7.65 (s, 1H), 7.57 (d, J = 7.5 Hz, 1H), 7.35–7.32 (m, 2H), 7.21 (d, J = 7.5 Hz, 2H), 6.95 (d, J = 8.1 Hz, 1H), 6.92 (d, J = 7.1 Hz, 2H), 6.88 (s, 1H), 6.83 (d, J = 2.2 Hz, 1H), 6.27 (dd, J = 3.4, 1.6 Hz, 1H), 6.25 (t, J = 3.1 Hz, 1H), 4.97 (s, 2H), 3.87 (s, 3H), 3.11 (s, 3H), 2.60 (s, 3H); **^{13}C NMR** (151 MHz, $CDCl_3$) δ (ppm): 169.14, 159.98, 157.96, 156.32, 140.60, 140.38, 137.49, 131.06, 129.55, 128.79, 128.78, 127.88, 127.37, 127.35, 123.98, 119.52, 115.02, 112.56, 110.71, 110.48, 109.06, 55.41, 51.25, 28.25, 26.80. **GC–MS** (EI) calculated for $C_{27}H_{24}N_4O_3$, 452.51 $[M]^+$; observed: 552.20.

2.2.21 | 5-(1-Benzyl-1*H*-Pyrrol-2-Yl)-7-(4-Chlorophenyl)-1,3-Dimethylpyrido[2,3-d] Pyrimidine -2,4(1*H*,3*H*)-Dione (2d)

Yield: 75%; yellow powder; **mp**: 158–160°C; **^{1}H NMR** (600 MHz, $CDCl_3$) δ (ppm): 7.91 (d, J = 8.6 Hz, 2H), 7.44 (d, J = 8.5 Hz, 2H), 7.34 (s, 1H), 7.18 (q, J = 6.7 Hz, 3H), 6.91 (d, J = 6.9 Hz, 2H), 6.88–6.85 (m, 1H), 6.33 (t, J = 3.1 Hz, 1H), 6.24 (dd, J = 3.5, 1.7 Hz, 1H), 4.96 (s, 2H), 3.84 (s, 3H), 3.44 (s, 3H); **^{13}C NMR** (151 MHz, $CDCl_3$) δ (ppm): 160.17, 158.19, 151.80, 151.52, 146.00, 138.03, 137.11, 135.64, 130.42, 129.22, 128.82, 128.58, 127.61, 127.21, 123.51, 119.55, 109.87, 108.55, 107.79, 51.59, 30.23, 28.65. **GC–MS** (EI) calculated for $C_{26}H_{21}ClN_4O_2$, 456.93 $[M]^+$; observed: 456.15.

2.2.22 | 5-(1-Benzyl-1*H*-Pyrrol-2-Yl)-1,3-Dimethyl-7-(*p*-Tolyl)Pyrido[2,3-d]Pyrimidine -2,4(1*H*,3*H*)-Dione (2e)

Yield: 80%; yellow powder; **mp**: 154–156°C; **^{1}H NMR** (600 MHz, $CDCl_3$) δ (ppm): 7.89 (d, J = 8.3 Hz, 2H), 7.38 (s, 1H), 7.28 (d, J = 8.0 Hz, 2H), 7.17 (dt, J = 15.0, 6.9 Hz, 3H), 6.92 (d, J = 7.1 Hz, 2H), 6.87–6.82 (m, 1H), 6.33 (t, J = 3.2 Hz, 1H), 6.24 (dd, J = 3.5, 1.7 Hz, 1H), 4.88 (s, 2H), 3.85 (s, 3H), 3.43 (s, 3H), 2.43 (s, 3H); **^{13}C NMR** (151 MHz, $CDCl_3$) δ (ppm): 160.30, 159.56, 151.75, 151.64, 145.59, 141.31, 138.05, 134.49, 130.72, 129.73, 128.57, 127.57, 127.52, 127.26, 123.21, 119.50, 109.61, 108.47, 107.35, 51.53, 30.18, 28.59, 21.52. **GC–MS** (EI) calculated for $C_{27}H_{24}N_4O_2$, 436.18 $[M]^+$; observed: 436.35; **HRMS** (TOF MS) calculated for $C_{27}H_{24}N_4O_2$, 437.1977 [M + H]; observed: 437.1968.

2.2.23 | 5-(1-Benzyl-1*H*-Pyrrol-2-Yl)-7-(2,4-Dibromophenyl)-1,3-Dimethylpyrido[2,3-d] Pyrimidine -2,4(1*H*,3*H*)-Dione (2f)

Yield: 80%; brown powder; **mp**: 162–164°C; **^{1}H NMR** (600 MHz, $CDCl_3$) δ (ppm): 7.88 (d, J = 8.6 Hz, 2H), 7.55 (d, J = 8.6 Hz, 2H), 7.49 (s, 1H), 7.14 (d, J = 2.2 Hz, 1H), 6.98–6.94 (m, 1H), 6.91 (s, 1H), 6.81 (d, J = 2.0 Hz, 1H), 6.35–6.30 (m, 1H), 6.29–6.26 (m, 2H), 4.97 (s, 2H), 3.10 (s, 3H), 2.62 (s, 3H); **^{13}C NMR** (151 MHz, $CDCl_3$) δ (ppm): 160.03, 158.00, 155.35, 148.49, 147.19, 139.75, 131.71, 130.48, 129.15, 128.79, 127.87, 127.27, 126.23, 124.20, 124.11, 114.65, 114.10, 110.77, 110.54, 110.07, 109.10, 51.04, 29.78, 28.26. **GC–MS** (EI) calculated for $C_{26}H_{20}Br_2N_4O_2$, 579.99 $[M]^+$; observed: 579.38.

2.2.24 | 5-(1-Benzyl-1*H*-Pyrrol-2-Yl)-7-(4-Fluorophenyl)-1,3-Dimethylpyrido[2,3-d] Pyrimidine -2,4(1*H*,3*H*)-Dione (2g)

Yield: 77%; yellow powder; **mp**: 164–164°C; **^{1}H NMR** (600 MHz, $CDCl_3$) δ (ppm): 7.99 (d, J = 3.1 Hz, 2H), 7.39–7.33 (m, 1H), 7.20 (d, J = 7.4 Hz, 2H), 7.09 (t, J = 8.7 Hz, 2H), 6.91 (d, J = 6.7 Hz, 2H), 6.83–6.81 (m, 1H), 6.81 (s, 1H), 6.27–6.24 (m, 2H), 4.96 (s, 2H), 3.09 (s, 3H), 2.60 (s, 3H); **^{13}C NMR** (151 MHz, $CDCl_3$) δ (ppm): 169.12, 164.61, 162.96, 158.01, 155.55, 140.51, 137.50, 135.20, 130.99, 128.92, 128.77, 127.86, 127.30, 124.04, 115.54, 115.39, 110.46, 109.97, 109.08, 51.24, 28.25, 26.82. **GC–MS** (EI) calculated for $C_{26}H_{21}FN_4O_2$, 440.47 $[M]^+$; observed: 440.35.

2.2.25 | 5-(1-Benzyl-1*H*-Pyrrol-2-Yl)-7-(3-Bromophenyl)-1,3-Dimethylpyrido[2,3-d] Pyrimidine -2,4(1*H*,3*H*)-Dione (2h)

Yield: 79%; yellow powder; **mp**: 156–158°C; **^{1}H NMR** (600 MHz, $CDCl_3$) δ (ppm): 8.14 (s, 1H), 7.91 (d, J = 7.9 Hz, 1H), 7.50 (d, J = 8.9 Hz, 1H), 7.33 (d, J = 4.7 Hz, 1H), 7.28 (t, J = 7.9 Hz, 1H), 7.21 (d, J = 7.4 Hz, 2H), 6.91 (d, J = 6.4 Hz, 2H), 6.84–6.83 (m, 1H), 6.82 (s, 1H), 6.28–6.24 (m, 2H), 4.96 (s, 2H), 3.10 (s, 3H), 2.60 (s, 3H); **^{13}C NMR** (151 MHz, $CDCl_3$) δ (ppm): 168.98, 163.16, 157.98, 154.90, 141.18, 140.51, 137.46, 132.13, 130.79, 130.10, 128.81, 127.93, 127.27, 126.98, 125.58, 124.17, 122.90, 111.18, 110.63, 110.37, 109.12, 51.30, 28.30, 26.82; **GC–MS** (EI) calculated for $C_{26}H_{21}BrN_4O_2$, 501.38 $[M]^+$; observed: [M + 1] 502.20.

2.2.26 | 5-(1-Benzyl-1H-Pyrrol-2-Yl)-7-(2,4-Dichlorophenyl)-1,3-Dimethylpyrido[2,3-d] Pyrimidine -2,4(1*H*,3*H*)-Dione (2i)

Yield: 69%; brown powder; **% Purity** ≥ 98 (HPLC); **mp**: 162–164°C; **^{1}H NMR** (600 MHz, $CDCl_3$) δ (ppm): 7.91 (d, J = 8.6 Hz, 2H), 7.44 (d, J = 8.6 Hz, 2H), 7.37 (s, 1H), 7.34 (s, 1H), 7.17 (d, J = 1.4 Hz, 1H), 6.92–6.91 (m, 2H), 6.84–6.81 (m, 1H), 6.35–6.32 (m, 1H), 6.24 (dd, J = 3.5, 1.7 Hz, 1H), 4.71 (s, 2H), 3.84 (s, 3H), 3.44 (s, 3H); **^{13}C NMR** (151 MHz, $CDCl_3$) δ (ppm): 168.98, 158.00, 154.89, 141.15, 140.49, 137.46, 132.13, 132.13, 130.78, 130.10, 128.81, 127.97, 127.93, 127.30, 125.58, 124.17, 122.90, 111.20, 110.65, 110.39, 109.11, 51.30, 28.33, 26.81. **GC–MS** (EI) calculated for $C_{26}H_{20}Cl_2N_4O_2$, 491.37 $[M]^+$; observed: 490.35.

2.2.27 | 5-(1-Benzyl-1*H*-Pyrrol-2-Yl)-7-(2-Chlorophenyl)-1,3-Dimethylpyrido[2,3-d] Pyrimidine -2,4(1*H*,3*H*)-Dione (2j)

Yield: 73%; yellow powder; **mp**: 158–160°C; **^{1}H NMR** (600 MHz, $CDCl_3$) δ (ppm): 7.69 (dd, J = 7.6, 1.7 Hz, 1H), 7.44 (dd, J = 7.8, 1.2 Hz, 1H), 7.33 (dd, J = 7.5, 1.3 Hz, 1H), 7.30 (dd, J = 7.7, 1.8 Hz, 1H), 7.22 (d, J = 5.8 Hz, 1H), 7.21–7.19 (m, 2H),

17470285, 2026, 1, Downloaded from https://onlinelibrary.wiley.com/doi/10.1111/cbdd.70240 by University Of Notre Dame, Wiley Online Library on [29/10/2026]. See the Terms and Conditions (https://onlinelibrary.wiley.com/terms-and-conditions) on Wiley Online Library for rules of use; OA articles are governed by the applicable Creative Commons License

6.95 (dd, J = 7.4, 1.6 Hz, 2H), 6.85 (d, J = 2.4 Hz, 1H), 6.85 (s, 1H), 6.23 (dd, J = 3.5, 1.8 Hz, 1H), 6.22–6.21 (m, 1H), 5.06 (s, 2H), 3.03 (s, 3H), 2.53 (s, 3H); **^{13}C NMR** (151 MHz, $CDCl_3$) δ (ppm): 169.10, 157.78, 156.08, 139.40, 139.16, 137.67, 132.31, 131.86, 130.59, 130.30, 129.59, 128.84, 128.58, 127.94, 127.39, 127.13, 126.96, 124.22, 114.78, 111.22, 109.03, 51.31, 28.33, 26.67. **GC–MS** (EI) calculated for $C_{26}H_{21}ClN_4O_2$, 456.93 $[M]^+$; observed: 456.15.

2.2.28 | 5-(1-Benzyl-1*H*-Pyrrol-2-Yl)-1,3-Dimethyl-7-(4-Nitrophenyl)Pyrido[2,3-d]Pyrimidine -2,4(1*H*,3*H*)-Dione (2k)

Yield: 77%; brown powder; **mp**: 164–166°C; **^{1}H NMR** (600 MHz, $CDCl_3$) δ (ppm): 7.85 (d, J = 8.7 Hz, 2H), 7.80 (d, J = 8.5 Hz, 2H), 7.29 (s, 1H), 7.06 (d, J = 7.4 Hz, 2H), 6.72–6.70 (m, 2H), 6.64 (d, J = 1.9 Hz, 1H), 6.63 (d, J = 1.9 Hz, 1H), 6.31–6.30 (m, 1H), 6.21 (dd, J = 3.5, 1.8 Hz, 1H), 5.25 (s, 2H), 3.82 (s, 3H), 3.41 (s, 3H); **^{13}C NMR** (151 MHz, $CDCl_3$) δ (ppm): 160.37, 159.53, 151.71, 149.33, 138.11, 130.82, 129.22, 128.55, 127.52, 127.31, 126.57, 122.93, 118.50, 117.61, 114.87, 113.98, 112.17, 110.07, 108.38, 51.46, 30.10, 28.52. **GC–MS** (EI) calculated for $C_{26}H_{21}N_5O_4$, 467.15 $[M]^+$; observed: 467.

3 | Biological Screening

3.1 | Cell Culture and Maintenance

To develop HCT 116, MCF-7, A549, and MDA-MB-231, DMEM medium comprising 10% Fetal Bovine Serum as well as 1% streptomycin and penicillin was utilized. It was stored at 37°C in an incubator having 5% CO_2 humidity. After trypsinizing the culture cells using 0.25% Trypsin–EDTA at approximately 70%–80% confluency, they were sub-cultured for additional research (Sarkar et al. 2017).

3.2 | Cytotoxicity Assay

The sensitivity of the medication to the cancerous cells (HCT 116, MCF-7, A549, and MDA-MB-231) was assessed using the MTT reagent in the cytotoxicity experiment. The assay principle was based on the reduction of yellow-colored 3-(4,5-dimethylthiazol-2-yl)-2,5-diphenyltetrazolium bromide (MTT) into dark purple, insoluble crystals of formazan. The cells were placed in 96-well plates (1×10^4 cells/well), left overnight at 37°C in a CO_2-humidified incubator, and then treated with different concentrations (1–25 μM) of synthesized compounds and raltitrexed for 24–48 h. At the final dose of 0.5 mg/mL of MTT, the treated cells underwent incubation for 4 h following the treatments. 200 μL of acidic DMSO was added to each well to disintegrate the purple crystals of formazan following the incubation time.

Carefully, the cell's culture medium was aspirated. The absorbance at 570 nm was measured using a microplate reader after the plates were left on a shaker for 10 to 20 min at room temperature. Untreated cells were used as a control. A positive control, Raltitrexed, was used. Each was measured three times. The findings were shown as mean ± SEM (Dhiman et al. 2012; Kumar et al. 2021).

3.3 | In Vitro Thymidylate Synthase Inhibitory Assay

An enzymatic analysis targeting thymidylate synthase was performed using the methodology of Wahba and Friedkin 1962, as well as Davisson et al. 1989. Elabscience supplied the hTS enzyme (catalog no. PKSH033115). Using a mixture containing 0.1 M 2-mercaptoethanol, 0.0003 M (6*R, S*)-tetrahydrofolate, 0.012 M formaldehyde, 0.02 M $MgCl_2$, 0.001 M dUMP, 0.04 M Tris–HCl, and 0.00075 M NaEDTA, thymidylate synthase was assayed spectrophotometrically at 30°C with pH 7.4. The process was initiated in the absence of an inhibitor by adding 30 nM hTS, which caused an absorbance variation of 0.019/min at 340 nm. After that, two inhibitor concentrations (1c, 2i) were used to calculate the inhibitor concentration. Then, a concentration–inhibition response graph for the test drugs was made in order to calculate the median inhibitory concentration (IC_{50}). Ratitrexed was used to compare the obtained results (Alam et al. 2020; Kumar et al. 2024).

3.4 | Molecular Docking

The high-resolution crystal structure of the target protein was obtained from the RCSB Protein Data Bank (PDB ID: 1HVY) (Phan et al. 2001), with a resolution of 1.90 Å. Only the biologically relevant monomeric unit (Chain A) was retained for subsequent computational analyses. All non-receptor entities—including co-crystallized ligands, water molecules, and other heteroatoms such as β-mercaptoethanol, raltitrexed (RAL), and inorganic ions—were systematically removed to avoid interference with docking accuracy. The only exception was the 2′-deoxyuridine 5′-monophosphate (dUMP) molecule, which was retained due to its covalent attachment to the sulfur atom of the Cys195 residue, representing a critical component of the active site.

Ligand structures were generated from their SMILES representations, followed by the generation of 10 low-energy conformers using the Merck Molecular Force Field (MMFF94) as implemented in RDKit (Tosco et al. 2014). The lowest-energy conformer was selected, converted to AutoDock-compatible .pdbqt format using the Meeko toolkit [https://github.com/forlilab/Meeko], and subsequently used in docking simulations. The protein receptor was prepared by retaining polar hydrogens and assigning partial atomic charges according to the Gasteiger method within ChimeraX (Meng et al. 2023).

Molecular docking was performed using AutoDock Vina (Eberhardt et al. 2021) with a grid box centered at the geometric center of the native ligand's binding site (coordinates: 1.97, 3.94, 13.77 Å). The grid dimensions were set to a cubic box of 30 Å per side to encompass the entire binding pocket and allow sufficient ligand mobility. Docking parameters included an exhaustiveness level of 100 and generation of up to 100 poses per ligand. Ligands were treated as fully flexible, allowing all rotatable bonds to be sampled. Post-docking analysis included energy-based ranking

17470285, 2026, 1, Downloaded from https://onlinelibrary.wiley.com/doi/10.1111/cbdd.70240 by University Of Notre Dame, Wiley Online Library on [29/10/2026]. See the Terms and Conditions (https://onlinelibrary.wiley.com/terms-and-conditions) on Wiley Online Library for rules of use; OA articles are governed by the applicable Creative Commons License

of the binding poses. All poses within 4 kcal/mol of the top-ranked conformation were retained for further consideration. To ensure methodological robustness, the docking protocol was validated by re-docking a known co-crystallized ligand, RAL.

3.5 | Molecular Dynamics Simulation

To investigate the dynamic behavior of the human thymidylate synthase (hTS) protein in complex with its ligand, an all-atom molecular dynamics (MD) simulation protocol was implemented using the AMBER 22 software suite (Case et al. 2023). The protein structure was modelled using the ff19SB force field (Tian et al. 2019), while protonation states of ionizable residues were determined at physiological pH (7.4) via the PDB2PQR web server (Dolinsky et al. 2004).

Ligand geometries were initially optimized at the MP2/6-31G* level of theory. Partial atomic charges were computed based on the Merz–Singh–Kollman scheme (Besler et al. 1990), derived from electrostatic potential calculations at the HF/6-31G* level. Subsequently, ligand parameters were generated using GAFF2 (Wang et al. 2004) through the Antechamber module within AMBER 22 (Wang et al. 2006).

Ligand–protein complexes obtained from molecular docking were placed at the center of a truncated octahedral periodic box, maintaining a buffer distance of 12 Å from any box edge. Solvation was performed using OPC water molecules (Onufriev and Izadi 2018). The systems were neutralized by the addition of Na^+ ions, with additional Na^+/Cl^- pairs introduced to mimic physiological salt conditions at 0.15 M (Machado and Pantano 2020).

Following the heating phase, equilibration was conducted for another 500 ps under constant pressure and temperature conditions. Production MD simulations were carried out for 150 ns using a 2 fs time step. Temperature control was achieved via the Langevin thermostat with a collision frequency of 1 ps^{-1}. All bonds involving hydrogen atoms were constrained using the SHAKE algorithm (Andersen 1983), allowing for a larger integration step. Periodic boundary conditions were applied in all directions, and long-range electrostatics were computed using the particle mesh Ewald (PME) method (Darden et al. 1993), with a non-bonded cut-off of 11 Å. To ensure statistical robustness, all simulations were conducted in triplicate. MD trajectories were processed and analyzed using pytraj (Roe and Cheatham III 2013). Simulations were executed on the Supek High-Performance Computing (HPC) cluster at the University Computing Center, University of Zagreb, Croatia.

3.6 | Binding Free Energy Calculation

To quantify the binding affinity between selected ligands and the 1HVY protein, the molecular mechanics/generalized Born surface area (MM/GBSA) approach was employed. This post-processing method, which avoids the need for explicit solvent molecules, efficiently decomposes the binding free energy (ΔG_{bind}) into molecular mechanics and solvation energy terms (Genheden and Ryde 2015). Binding free energy estimations were carried out using the MMPBSA.py module, a component of AmberTools, utilizing the single-trajectory protocol, where snapshots of the complex, receptor, and ligand are extracted from the same MD trajectory. The binding free energy was computed using the equation:

$$\Delta G_{bind} = \Delta H - T\Delta S \quad (1)$$

$$\Delta E_{MM} = \Delta E_{internal} + \Delta E_{electrostatic} + \Delta E_{vdW} \quad (2)$$

$$\Delta G_{sol} = \Delta G_{GB} + \Delta G_{SA} \quad (3)$$

ΔE_{MM} represents the gas-phase molecular mechanics energy, incorporating $\Delta E_{internal}$ (bond, angle, dihedral energies), $\Delta E_{electrostatic}$, and ΔE_{vdW} (van der Waals interactions). ΔG_{sol}, the solvation free energy, is comprised of ΔG_{GB}, the electrostatic solvation term estimated via the generalized Born (GB) model, ΔG_{SA}: the non-polar solvation contribution estimated from solvent-accessible surface area, reflecting hydrophobic effects. The entropic contribution (–TΔS), though optional due to its high computational cost, was estimated to account for conformational entropy changes upon binding.

To ensure robust statistical averaging and comprehensive sampling, each 300 ns MD trajectory was divided into six 50 ns segments. From each segment, 50 equally spaced snapshots were extracted, totaling 300 snapshots per simulation. Given that all simulations were performed in triplicate, the final analysis encompassed 900 snapshots in total. Binding free energies (ΔG_{bind}) were computed for each snapshot, and the final values were reported as mean ± standard deviation across the full dataset.

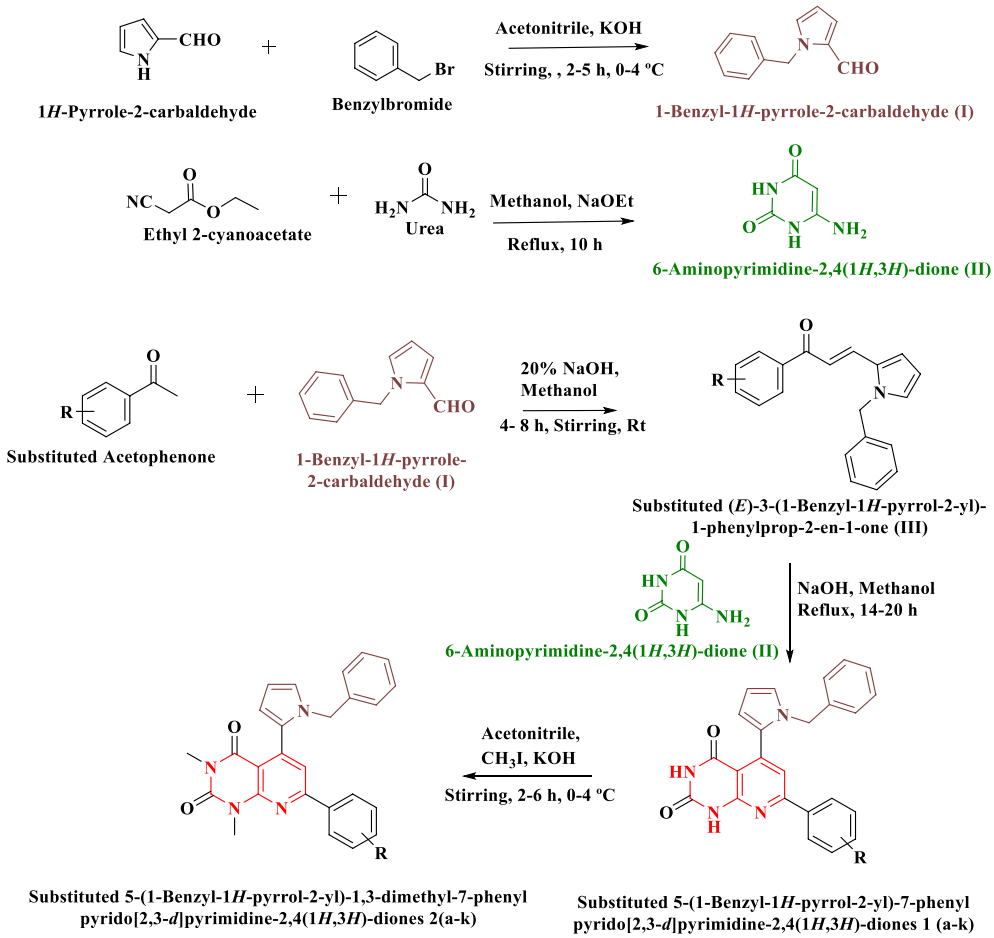
3.7 | ADME (Physical, Chemical, Biochemical, and Toxicological) Investigations

A rapid and simple method for estimating ligand process of absorption, distribution, metabolism, as well as elimination properties is the QikProp module of the Schrodinger suite. Prepared ligands were used to measure the ADME characteristics. The features of compounds that are relevant to medications and their physically significant descriptors are accurately predicted by it. The analysis's prepared molecules were loaded from the file, and the job was told to run. Polar Surface Area (PSA), QPlogHERG, QPPMDCK, QPlogP(o/w), QPlogBB, QPPCaco, QPlogKp, acceptor as well as donor hydrogen bonds, ligand molecular weight, and the proportion of oral absorption by humans have all been evaluated in relation to pharmacokinetic properties. The basic concept and physiological properties of inhibitors can be predicted with the help of Lipinski's rule (Bisht Gunjan et al. 2022; Kumar, Novak, et al. 2023).

4 | Results and Discussion

As illustrated in Scheme 1, a total of 22 benzylated pyrrole-based pyrido[2,3-d]pyrimidine and alkylated pyrido[2,3-d] pyrimidines **1 (a–k)** and **2 (a–k)** were synthesized. Initially, various substituted acetophenones were reacted with benzylated pyrrole carbaldehyde (I) in the presence of NaOH to yield the

17470285, 2026, 1, Downloaded from https://onlinelibrary.wiley.com/doi/10.1111/cbdd.70240 by University Of Notre Dame, Wiley Online Library on [29/10/2026]. See the Terms and Conditions (https://onlinelibrary.wiley.com/terms-and-conditions) on Wiley Online Library for rules of use; OA articles are governed by the applicable Creative Commons License



SCHEME 1 | Synthetic procedure of benzylated pyrrole-based pyrido[2,3-d]pyrimidines **1 & 2 (a–k)**.

corresponding substituted chalcones. These chalcones were then subjected to a cyclization reaction with 6-aminopyrimidine-2,4 (1H,3H)-dione (II) to afford the benzylated pyrrole-based pyrido[2,3-d]pyrimidines **1(a–k)**. Subsequently, these compounds were alkylated using methyl iodide to yield the N-methylated analogs, that is, benzylated pyrrole-based alkyl-substituted pyrido[2,3-d]pyrimidines **2(a–k)**.

The successful alkylation at the NH position of the pyrido[2,3-d] pyrimidine ring was confirmed by the appearance of two methyl singlets in the range of 2.0–3.7 ppm in the ^{1}H NMR spectra and corresponding signals between 20 and 32 ppm in the ^{13}C NMR spectra. Furthermore, the two carbonyl carbon signals of the alkyl-substituted pyrido[2,3-d]pyrimidines were observed in the range of 156–177 ppm in the ^{13}C NMR spectra, confirming the presence of the pyrimidine-2,4-dione moiety. Moreover, the presence of fluorine in the compounds can be seen in ^{1}H NMR spectra also as the J values indicated the ortho and meta H-F coupling [7.39–7.33 (m, 1H), 7.99 (d, J = 3.1 Hz, 2H) respectively] in compound 2g and for 1g, ortho H-F couplings [8.11 (dd, J = 8.8, 5.6 Hz, 2H)] were observed. The peak of ipso C-F in ^{13}C was be observed for compound 2g at 164.61 ppm and because of low signal intensity and line broadening caused by NH-induced exchange effects, this peak is not present in 1g. Further, bromine-containing compounds (1a, 1f, 1h, 2a, 2f and 2h) and chlorine-containing compounds (1d, 1i, 1j, 2d, 2i, and 2j) have isotopic peaks in their mass spectrum except 1f because of poor stability of the molecular ion and facile C–Br bond cleavage during ionization, leading to dominant debrominated fragment ions rather than the intact molecular ion. All synthesized compounds were thoroughly characterized using ^{1}H NMR, ^{13}C NMR, GC–MS (EI), HRMS, HPLC, and by determining their melting points (Figures S1–S71).

5 | Biological Assessment

5.1 | In Vitro Cytotoxicity Activity

The cytotoxic activity of the synthesized compounds was evaluated against four human cancer cell lines including HCT 116 (colorectal), MCF-7 (breast cancer), A549 (lung), and MDA-MB-231 (triple-negative breast cancer) to explore structure–activity relationships (SAR) based on varying substitution patterns. The compounds are divided into two major series: Series 1 (1a–1k), which features unsubstituted amines, and Series 2 (2a–2k), which includes N,N-dimethyl substitution. Overall, it was observed that both the nature and position of the substituent on the aromatic ring significantly influenced the anticancer activity, with some derivatives displaying potent and selective cytotoxic profiles.

Among series 1, compound 1c (3-methoxy substitution) exhibited the lowest IC_{50} in HCT 116 (IC_{50} = 1.10 μM), A549 (2.25 μM), and

17470285, 2026, 1, Downloaded from https://onlinelibrary.wiley.com/doi/10.1111/cbdd.70240 by University Of Notre Dame, Wiley Online Library on [29/10/2026]. See the Terms and Conditions (https://onlinelibrary.wiley.com/terms-and-conditions) on Wiley Online Library for rules of use; OA articles are governed by the applicable Creative Commons License

MCF-7 (3.06 μM), suggesting a critical role for the meta-methoxy group in enhancing cell permeability or target interaction. In contrast, its isomer 1b (4-methoxy) showed drastically reduced potency in HCT 116 (IC_{50} = 4.11 μM), indicating that positional effects of the methoxy group are highly influential, possibly due to steric hindrance or altered electronic effects disrupting favorable binding. Halogen substitutions at the para-position, such as 4-bromo (1a) and 4-chloro (1d), also exhibited commendable activity, especially in HCT 116 and A549 cells, reinforcing the importance of electron-withdrawing groups in enhancing anticancer potency. However, compounds with bulkier or multiple halogens, such as 1f (2,4-dibromo) and 1i (2,4-dichloro), demonstrated moderate to poor activity in most cell lines, potentially due to steric hindrance affecting cellular uptake or target affinity. Furthermore, compound 1e (4-methyl) showed only moderate potency, implying that electron-donating alkyl groups were less favorable than halogens.

Series 2 compounds, which are *N,N*-dimethyl derivatives, revealed interesting trends. Notably, compound 2i (2,4-dichloro) demonstrated strong cytotoxic activity across all cell lines (IC_{50} = 1.91–5.32 μM), even the reference drug raltitrexed, suggesting that combined electron-withdrawing substitutions and *N,N*-dimethylation synergistically enhanced biological activity. Similarly, 2d (4-chloro) and 2f (2,4-dibromo) retained good activity in HCT 116 and MCF-7, indicating that halogenation remains a critical factor for potency, even after methyl substitution. On the contrary, 2b and 2c (methoxy derivatives) exhibited reduced cytotoxicity compared to their Series 1 counterparts, indicating that N,N-dimethylation negatively affects the activity of electron-donating groups.

From a cell line perspective, HCT 116 was the most responsive, with several compounds (1c, 2i, 2d, and 2f) showing IC_{50} values below 3 μM, whereas MDA-MB-231 exhibited the greatest resistance, highlighting the difficulty in targeting triple-negative breast cancer with these scaffolds. Overall, the results suggested that electron-withdrawing halogens at the para- or 2,4-positions, particularly chlorine and bromine, enhanced cytotoxic activity, and meta-substituted methoxy groups could be highly favorable in the absence of N,N-dimethylation. The impact of N,N-dimethylation is beneficial in some halogenated structures but detrimental in methoxy or alkyl-substituted compounds (Table 1).

5.2 | Structure–Activity Relationship

a. The structure–activity relationship (SAR) analysis of the synthesized compounds against the tested cell lines revealed that the pyrido[2,3-d]pyrimidine pharmacophore is crucial for anticancer activity, which is consistent with the findings reported by Kumar, Bhagat, et al. (2023).

5.2.1 | Substitution Patterns

All compounds belong to two series: 1 (1a–1k), which features unsubstituted amines, and series 2 (2a–2k), which includes N,N-dimethyl substitution, allowing us to assess the effect of N,N-dimethyl substitution on cytotoxicity. The R group varies with different electron-donating (e.g., methoxy, methyl) and electron-withdrawing (e.g., halogens, nitro) substituents.

5.2.1.1 | Series 1 (1a–1k): Unsubstituted Amines.

I. 3-Methoxy (1c) showed the most potent activity, particularly in HCT 116 (1.10 μM), MCF-7 (3.06 μM), and A549 (2.25 μM). This suggests favorable interaction of the meta-methoxy group with biological targets.

II. 4-Bromo (1a) also exhibited strong activity, notably in HCT 116 (3.89 μM) and A549 (4.52 μM).

III. Electron-withdrawing halogens (Cl, Br) at the para-position (1a, 1d) were generally more active than alkyl (1e) or fluoro (1g).

IV. Compound 1b (4-methoxy) was highly active in HCT 116 (IC_{50} = 4.11 μM), implying that para-methoxy was favorable to activity against this cell line.

V. Dihalogen substitution (1f: 2,4-dibromo; 1i: 2,4-dichloro) led to moderate to poor activity, especially in MCF-7 and MDA-MB-231, possibly due to steric hindrance.

5.2.1.2 | Series 2 (2a–2k): N,N-Dimethyl Substitution.

I. This series introduces N,N-dimethyl substitutions, which impact electronic and steric properties. Improved activity was seen in some analogues (e.g., 2d, 2i) upon methyl substitution compared to their Series 1 counterparts.

II. Compound 2i (2,4-dichloro) is notably active across all lines: HCT 116 (1.91 μM), MCF-7 (3.12 μM), A549 (4.48 μM), and MDA-MB-231 (5.32 μM). This indicates that di-chlorination and N,N-dimethylation enhance cytotoxicity.

III. Compound 2d (4-chloro) also maintained good activity in HCT 116 and MCF-7.

IV. 4-bromo substitution (compound 2a) retained similar potency as 1a, showing that dimethylation didn't alter activity significantly.

V. Compound 2f (2,4-dibromo) maintained reasonable activity in HCT 116 (2.36 μM) but was weaker in other lines.

VI. Methoxy groups (2b and 2c) showed reduced potency relative to 1b and 1c, indicating that N,N-dimethylation likely diminishes the favorable interactions of these groups.

5.2.2 | Cell Line-Specific Activity Trends

i. HCT 116 (Colorectal Cancer) was most responsive overall, particularly to compounds 1c, 2i, 2d, and 2f. Compounds with meta-substitution (e.g., 3-methoxy, 3-bromo) or multiple halogens tend to work better.

ii. MCF-7 (Breast Cancer) was responsive to compounds 1c, 2i, 2d, and 1a. Again, halogen substitutions, especially 4-chloro and 2,4-dichloro, contributed to enhanced potency.

iii. A549 (Lung Cancer) showed good sensitivity to compounds 1c, 1a, 2i, and 2k (4-nitro), indicating preference for electron-withdrawing groups.

17470285, 2026, 1, Downloaded from https://onlinelibrary.wiley.com/doi/10.1111/cbdd.70240 by University Of Notre Dame, Wiley Online Library on [29/10/2026]. See the Terms and Conditions (https://onlinelibrary.wiley.com/terms-and-conditions) on Wiley Online Library for rules of use; OA articles are governed by the applicable Creative Commons License

TABLE 1 | Anticancer activity of synthesized compounds (1a–k & 2a–k).

Comp.	R	HCT 116	MCF-7	A549	MDA-MB-231
IC_{50} μM[a]					
1a	4-Bromo	3.89 ± 1.06	6.38 ± 1.27	4.52 ± 1.02	8.78 ± 1.67
1b	4-Methoxy	4.11 ± 1.01	7.40 ± 1.10	6.10 ± 1.19	6.63 ± 0.91
1c	**3-Methoxy**	**1.10 ± 0.61**	**3.06 ± 1.25**	**2.25 ± 1.73**	**4.01 ± 0.05**
1d	4-Chloro	2.23 ± 0.93	8.14 ± 0.78	13.15 ± 1.91	11.34 ± 0.71
1e	4-Methyl	4.95 ± 0.78	10.7 ± 0.94	7.98 ± 1.92	10.61 ± 1.59
1f	2,4-Dibromo	2.39 ± 1.02	20.69 ± 1.64	15.57 ± 1.02	19.89 ± 1.31
1g	4-Fluoro	11.44 ± 1.71	10.48 ± 1.58	4.00 ± 1.58	19.10 ± 1.69
1h	3-Bromo	3.07 ± 0.48	16.98 ± 0.98	7.43 ± 1.03	18.98 ± 0.76
1i	2,4-Dichloro	2.15 ± 1.32	13.50 ± 1.29	14.54 ± 1.18	12.50 ± 1.86
1j	2-Chloro	9.03 ± 1.28	5.51 ± 1.64	17.25 ± 1.52	15.51 ± 1.14
1k	4-Nitro	5.10 ± 1.21	7.71 ± 1.19	11.06 ± 1.75	13.71 ± 1.09
2a	4-Bromo	3.50 ± 1.98	5.50 ± 1.39	8.61 ± 1.06	8.50 ± 1.87
2b	4-Methoxy	7.79 ± 1.05	11.09 ± 1.07	9.62 ± 1.72	17.09 ± 1.07
2c	3-Methoxy	6.90 ± 1.90	14.76 ± 1.63	11.02 ± 0.09	19.46 ± 1.23
2d	4-Chloro	2.56 ± 0.89	3.84 ± 0.87	13.18 ± 1.33	10.64 ± 0.69
2e	4-Methyl	10.20 ± 0.83	14.06 ± 1.06	16.11 ± 1.06	17.16 ± 0.87
2f	2,4-Dibromo	2.36 ± 0.66	11.35 ± 1.21	10.17 ± 1.44	18.05 ± 0.92
2g	4-Fluoro	9.49 ± 1.60	9.51 ± 1.57	9.21 ± 1.07	14.61 ± 1.15
2h	3-Bromo	8.55 ± 1.06	5.43 ± 1.48	11.20 ± 0.84	9.13 ± 0.64
2i	**2,4-Dichloro**	**1.91 ± 1.55**	**3.12 ± 1.59**	**4.48 ± 1.95**	**5.32 ± 1.06**
2j	2-Chloro	10.23 ± 1.07	14.54 ± 1.09	10.62 ± 1.06	18.06 ± 1.06
2k	4-Nitro	8.74 ± 0.78	11.51 ± 1.46	5.33 ± 1.09	15.11 ± 0.84
Raltitrexed	—	1.29 ± 0.84	2.27 ± 1.02	2.98 ± 0.07	4.17 ± 0.72

Note: Bold compounds are having potent activity over other synthetics.
[a]Data are presented as mean ± standard error of the mean (SEM) from three independent experiments.

iv. MDA-MB-231 (Triple-negative breast cancer) was least responsive overall. Most promising compounds were 1c, 2i, and 2d.

Overall, the compound 1c (3-Methoxy) was potent across all cell lines, especially HCT 116 and A549, 2i (2,4-Dichloro, N,N-dimethyl) was strongest across all four cell lines, 2d (4-Chloro, N,N-dimethyl) showed high potency in HCT 116 and MCF-7, and compound 1a (4-Bromo) was consistently good in HCT 116 and A549 (Figure 1).

5.3 | In Vitro Thymidylate Synthase (TS) Inhibitory Activity

In vitro TS inhibition data revealed that compound 1c exhibited the highest potency with an IC_{50} of 11.50 ± 1.08 nM, slightly potent than the clinically used TS inhibitor raltitrexed (IC_{50} = 12.51 ± 0.91 nM). Compound 2i showed moderate TS inhibition with an IC_{50} of 17.12 ± 0.91 nM, remaining within the low nano-molar range. These results suggested that compound 1c is promising lead candidate for further development as a TS-targeted anticancer agent, given its comparable or slightly superior efficacy to raltitrexed. Compound 1c and 2i were structural analogues, their differences in activity may result from: variations in functional groups affecting binding affinity to TS active site, differences in lipophilicity or molecular conformation and potential steric hindrance or electronic effects influencing their enzyme interaction (Table 2).

5.4 | Analysis of Docking and Molecular Dynamics Simulation

Molecular docking simulations yielded well-defined binding poses for all investigated ligands within the active site of the 1HVY protein. To validate the docking protocol, the co-crystallized ligand (2*S*)-2-[(5-{methyl[(2-methyl-4-oxo-1,4-dihydroquinazolin-6-yl)methyl]amino}thiophen-2-yl)formamido]pentanedioic acid (RAL) was re-docked into the active site of the 1HVY protein

17470285, 2026, 1, Downloaded from https://onlinelibrary.wiley.com/doi/10.1111/cbdd.70240 by University Of Notre Dame, Wiley Online Library on [29/10/2026]. See the Terms and Conditions (https://onlinelibrary.wiley.com/terms-and-conditions) on Wiley Online Library for rules of use; OA articles are governed by the applicable Creative Commons License

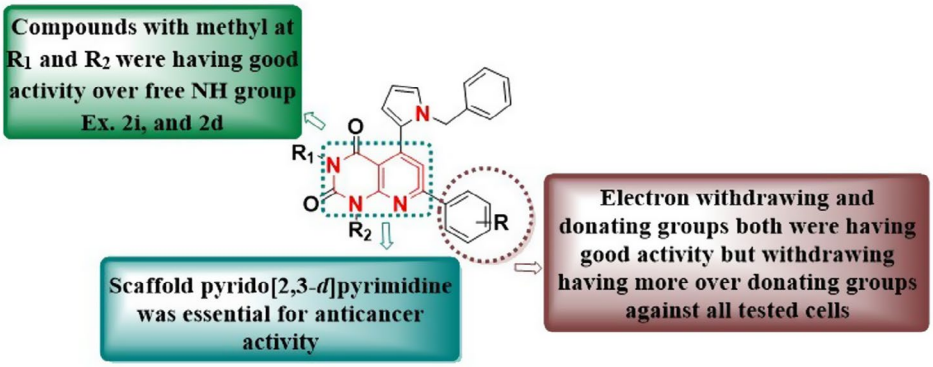


FIGURE 1 | Structure–activity relationship based on anticancer activity of synthesized compounds.

TABLE 2 | Thymidylate synthase (TS) inhibitory activity of compounds 1c and 2i.

Compound No.	IC_{50} (nM) ± SEM[a]
1c	11.50 ± 1.08
2i	17.12 ± 0.91
Raltitrexed	12.51 ± 0.91 nM

[a]Data are presented as mean ± standard error of the mean (SEM) from three independent experiments.

(Figure S72). The third-ranked pose, with a docking score of −9.167 kcal·mol^{-1}, exhibited an RMSD of 5.151 Å compared to the crystallographic pose. While this RMSD indicates a moderate deviation, most key interactions—such as hydrogen bonds and aromatic stacking within the binding pocket—were maintained. The primary difference between the docked and crystallographic conformations was the reorientation of the pentanedioic acid moiety, which adopted a distinct binding orientation. Despite this variation, the preservation of critical contacts suggests the docking protocol reliably captures relevant binding interactions.

All compounds demonstrated favorable docking scores, indicative of energetically stable complexes, with key interactions involving conserved residues within the active site. Hydrophobic and van der Waals contacts were consistently observed across top-ranked poses, suggesting a good geometric and chemical complementarity between the ligands and the binding pocket (Figure S73). Notably, all synthesized compounds exhibited more favorable docking scores than the reference drug RAL, highlighting their promising binding potential and supporting their selection for subsequent molecular dynamics simulations and binding free energy calculations (Table SI1).

The radar plot presents a comparative visualization of the Lipinski's Rule of Five (Ro5) parameters for three molecules: 1C, 2I, and RAL (Figure S74). The Ro5 guidelines suggest that drug-like compounds are more likely to exhibit good oral bioavailability when they meet the following criteria: molecular weight ≤ 500 Da, ≤ 5 hydrogen bond donors (HBD), ≤ 10 hydrogen bond acceptors (HBA), and a log octanol–water partition coefficient (log P) ≤ 5. In the plot, molecular weight is scaled by a factor of 100, HBA and rotatable bonds (ROT) are scaled by 2, while HBD and log P are presented as it is to allow for a more balanced comparative view. 1C and 2I showed parameter values that fell well within the recommended thresholds, indicating strong compliance with Ro5 and suggesting favorable oral drug-like properties. In contrast, RAL displayed deviations in at least one parameter—most notably, a higher molecular weight—potentially suggesting reduced suitability for oral administration. However, this limitation is clinically irrelevant in the case of RAL, as it is already an established chemotherapeutic agent administered via intravenous infusion. Thus, while RAL may not conform fully to Ro5, its efficacy via parenteral administration circumvents the predictive constraints of the rule, underscoring that Ro5 is primarily applicable to orally administered agents. This highlights the need to consider the intended route of administration when interpreting drug-likeness metrics.

To assess the structural stability of the hTS complexes with compounds 1C, 2I, and RAL, we performed root mean square deviation (RMSD) analysis of backbone atoms over 300 ns molecular dynamics (MD) simulations in triplicate. The time evolution of RMSD is shown in Figure 2. RMSD is a fundamental metric used in molecular dynamics simulations to quantify the average positional deviation of atoms—typically backbone atoms—from a reference structure (the starting conformation). In computational drug discovery, RMSD is critical for evaluating the dynamic stability of protein–ligand complexes, identifying potential binding-induced conformational changes, and validating convergence of simulation trajectories.

Stable RMSD values suggest that the system has equilibrated and that the binding pocket and global protein fold are preserved over time. Conversely, large fluctuations may indicate flexibility, binding pose instability, or transitions to alternative conformations, which may impact ligand binding efficacy and pharmacodynamic behaviour. 1C exhibited the most stable RMSD profiles, suggesting tight and consistent binding across replicates. 2I showed stable behaviour in two replicates, but the third replicate revealed conformational drift, potentially indicative of partial unbinding or induced fit-like motion. RAL-bound hTS displayed the highest variability, with marked RMSD fluctuations across all three replicates.

As shown in Figure 2 and Table 3, all systems maintained overall structural stability throughout the simulations. Average backbone RMSD values ranged from 1.77 ± 0.56 Å for hTS:C2I to 2.33 ± 0.63 Å for hTS:RAL, suggesting moderate deviations from

17470285, 2026, 1, Downloaded from https://onlinelibrary.wiley.com/doi/10.1111/cbdd.70240 by University Of Notre Dame, Wiley Online Library on [29/10/2026]. See the Terms and Conditions (https://onlinelibrary.wiley.com/terms-and-conditions) on Wiley Online Library for rules of use; OA articles are governed by the applicable Creative Commons License

the initial structures. The lowest RMSD observed for hTS:C2I points to increased structural rigidity, while the higher average and variance in the RAL complex reflect greater conformational flexibility. The 1C complex (2.05 ± 0.38 Å) demonstrated intermediate stability, suggesting a well-bound but dynamically responsive system.

To further probe structural integrity, we evaluated the radius of gyration (R_g), a global descriptor of protein compactness (Figure S75). All complexes retained a consistent R_g, with values of 19.0 ± 0.1 Å for both hTS:C1C and hTS:C2I, and 19.2 ± 0.2 Å for hTS:RAL. These results support the RMSD findings, with RAL-bound hTS showing a slight tendency toward expansion. Although subtle, the increased R_g suggests marginal loosening of the protein structure, which may correlate with increased flexibility or ligand-induced conformational adaptation.

The solvent-accessible surface area (SASA) complements this picture by quantifying the extent of protein surface exposure to the solvent (Figure S76). The hTS:RAL complex displayed the highest SASA (13,482 ± 430 Å^2), followed by hTS:C2I (13,310 ± 243 Å^2) and hTS:C1C (13,307 ± 251 Å^2). The elevated SASA in the presence of RAL implies greater solvent exposure, which aligns with the R_g and RMSD trends. Interestingly, hTS:C2I maintained both low RMSD and low SASA, suggesting that this ligand favors a more stable and compact protein conformation.

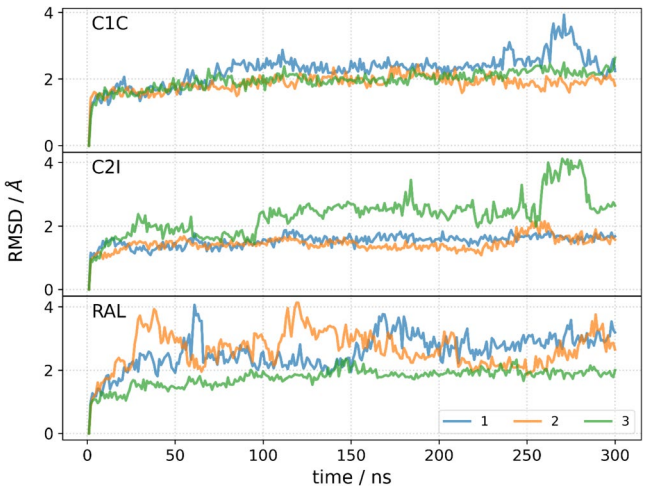


FIGURE 2 | Root mean square deviation (RMSD) profiles of three ligand–hTS complexes over the course of molecular dynamics simulations.

To investigate residue-specific flexibility and identify regions of local conformational mobility, we analyzed the root mean square fluctuation (RMSF) of Cα atoms for each hTS–ligand complex across three independent MD replicates (Figure S77). Overall, the RMSF profiles revealed similar fluctuation patterns across all complexes, characterized by relatively stable backbone regions and increased mobility in terminal segments and loops. As anticipated, the *N*-terminal (Pro26-His28) and *C*-terminal (Met309-Val313) residues consistently showed the highest fluctuations, reflecting their inherent structural flexibility (Figure S78).

In addition to the termini, two conserved regions exhibited elevated fluctuations—Asp48–Thr53, corresponding to a β-hairpin linking two β-sheets, and the segment around Asp173, connecting an α-helix and a β-strand. These segments showed RMSF values approximately twice the average, and this trend was observed in at least two out of three replicates for all complexes. Importantly, these regions are located distal to the active site and do not interact directly with the ligands, suggesting that their flexibility is inherent to the protein architecture rather than ligand-induced. Among the three systems, the hTS:RAL complex displayed the highest average RMSF (1.28 ± 1.00 Å), indicating increased local and global flexibility. While the overall RMSF profile resembled that of the other two complexes, triplicate 2 exhibited a noticeable increase in mobility within the Asp116-Thr125 loop, a region not observed to fluctuate significantly in the other simulations. This observation is in line with the elevated RMSD, Rg, and SASA values previously discussed, reinforcing the conclusion that RAL binding induces greater structural plasticity in hTS.

Conversely, the hTS:1C and hTS:2I complexes exhibited comparable average RMSF values (1.18 Å and 1.17 Å, respectively), with consistently low fluctuations across all replicates. Flexibility remained especially limited in central structural domains, suggesting that binding of 1C and 2I promotes conformational stabilization of the protein. These findings are consistent with the lower RMSD, more compact R_g, and reduced SASA, supporting more rigid, stable protein architecture upon ligand binding.

The analysis of cumulative interaction profiles for the C1C, C2I, and RAL complexes revealed distinct patterns in the nature and distribution of key ligand–protein contacts. In the hTS:C1C complex, interactions were predominantly driven by hydrophobic contacts and van der Waals (vdW) interactions, involving residues such as Phe225, Leu221, Ile108, and Phe80, all exceeding 70% interaction frequency. Notably, π-stacking interactions were significant with Phe225 and Phe80, and a moderate H-bond acceptor interaction was detected with Phe80. In contrast,

TABLE 3 | Summary of structural stability metrics for hTS complexes with 1C, 2I, and RAL ligands.[a]

Complex	RMSD/Å	R_g/Å	SASA/Å^2	RMSF/Å
hTS:1C	2.05 ± 0.38	19.0 ± 0.1	13,307 ± 251	1.18 ± 0.76
hTS:2I	1.77 ± 0.56	19.0 ± 0.1	13,310 ± 243	1.17 ± 0.79
hTS:RAL	2.33 ± 0.63	19.2 ± 0.2	13,482 ± 430	1.28 ± 1.00

[a]Reported values represent the mean ± standard deviation of backbone root mean square deviation (RMSD), radius of gyration (R_g), solvent-accessible surface area (SASA), and root mean square fluctuation (RMSF), averaged over triplicate MD simulations.

17470285, 2026, 1, Downloaded from https://onlinelibrary.wiley.com/doi/10.1111/cbdd.70240 by University Of Notre Dame, Wiley Online Library on [29/10/2026]. See the Terms and Conditions (https://onlinelibrary.wiley.com/terms-and-conditions) on Wiley Online Library for rules of use; OA articles are governed by the applicable Creative Commons License

the hTS:C2I complex exhibited a more even distribution of interaction types. While hydrophobic and vdW contacts remained dominant (particularly with Ala111, Phe117, and Met311), Thr51 and Asn112 uniquely contributed via hydrogen bonding (H-bond acceptor and donor roles), suggesting an increased polarity of interaction compared to 1C. The 2I interaction profile indicated a broader engagement across both hydrophobic and polar residues, which may imply enhanced binding stability through diversified contact types.

The hTS:RAL complex displayed a markedly different interaction pattern, characterized by a stronger contribution from polar interactions, including π-stacking (notably with Arg50) and significant H-bond acceptor/donor interactions (especially at Tyr258 and Arg50). While Ile108, Leu221, and Phe225 continued to mediate hydrophobic and vdW contacts, RAL uniquely engaged several polar residues absent in the top 1C and 2I profiles. Interestingly, Tyr258, absent from the primary interaction list for 1C and 2I, was a major interaction partner for RAL, implying a different binding orientation. Collectively, 1C and 2I favoured hydrophobic stabilization via a more conventional binding mode, while RAL promoted enhanced conformational adaptability and polarity-driven interactions, consistent with its observed greater influence on protein flexibility and higher RMSF/RMSD values (Figure 3). This shift in interaction nature may have important implications for the binding affinity, specificity, and dynamic modulation of hTS activity by these ligands.

The molecular mechanics/generalized Born surface area (MM/GBSA) approach is widely used for estimating binding free energies due to its favorable balance between computational efficiency and reasonable accuracy. Its advantages include the ability to process large datasets and extract binding trends from molecular dynamics simulations without requiring extensive alchemical transformations. However, it comes with notable limitations, particularly in handling entropic contributions and conformational variability. Entropy is typically estimated through input structures and simulation sampling. Moreover, MM/GBSA is a snapshot-based post-processing technique and does not inherently account for long-timescale dynamics or rare binding events. These aspects can lead to discrepancies with experimental affinities, especially for flexible ligands or dynamic binding sites (Genheden and Ryde 2015; Hou et al. 2011).

5.5 | Analysis of Binding Free Energy Calculation

In this study, MM/GBSA calculations including entropy corrections were performed on three ligands—1C, 2I, and RAL—bound to the same protein target. Each system was simulated in triplicate, and binding free energy estimates (ΔG_{bind}) were averaged over all triplicates. The averaged binding energies (Table 4) are for 10 kcal mol^{-1} higher for hTS:1C and hTS:2I, compared to hTS:RAL, before inclusion of the entropic term (TΔS). The vibrational entropy contribution (TΔS) from MD snapshots was calculated using normal mode analysis within the GB implicit solvent model. Entropy correction was more substantial for the hTS:RAL complex, reducing the gap of the final Δ*Gbind* by 3 kcal mol^{-1}.

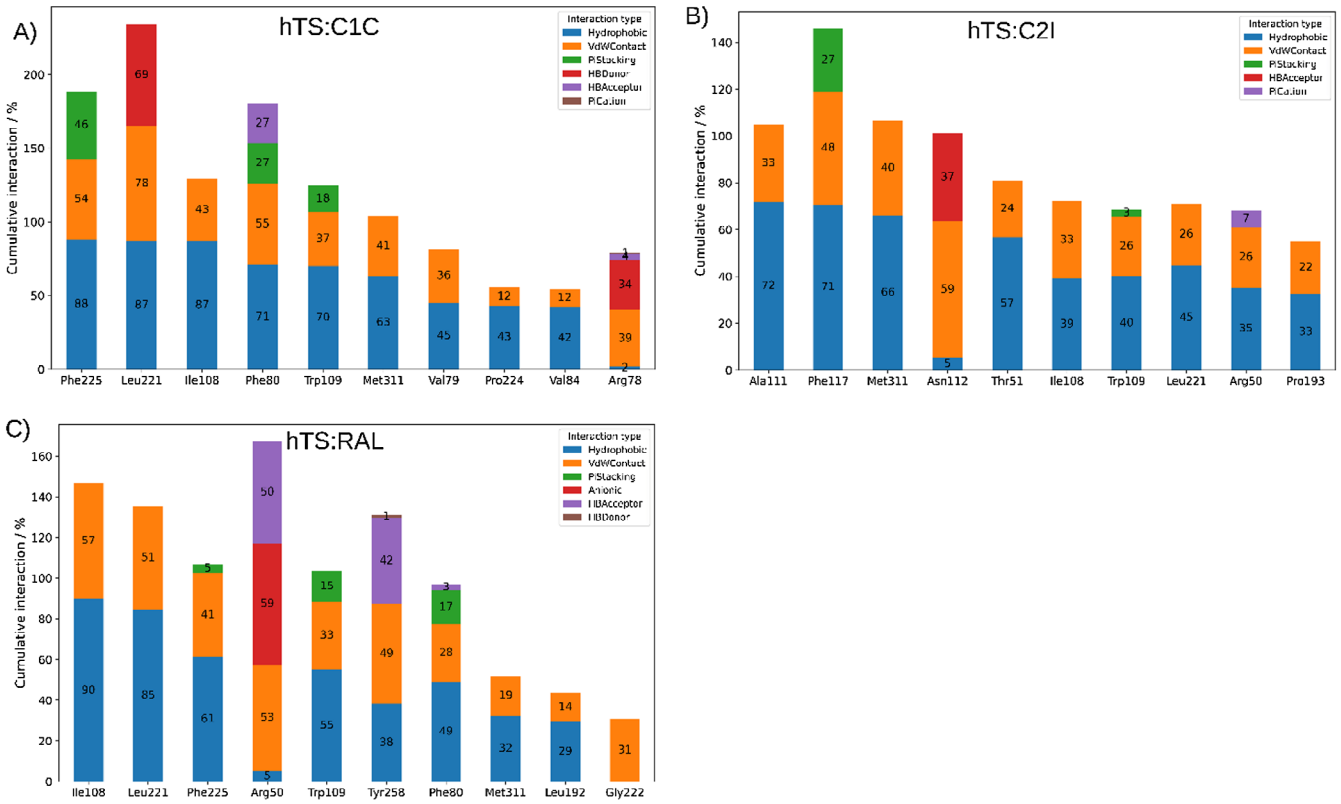


FIGURE 3 | Top 10 protein residues involved in ligand binding, ranked by cumulative interaction frequency across the simulation trajectory. Bars represent the total interaction contribution per residue, with colors indicating different interaction types. (A) hTS and compound 1c; (B) hTS and compound 2i; and (C) hTS and RAL.

17470285, 2026, 1, Downloaded from https://onlinelibrary.wiley.com/doi/10.1111/cbdd.70240 by University Of Notre Dame, Wiley Online Library on [29/10/2026]. See the Terms and Conditions (https://onlinelibrary.wiley.com/terms-and-conditions) on Wiley Online Library for rules of use; OA articles are governed by the applicable Creative Commons License

Triplicate-averaged binding free energy estimates demonstrated consistent ligand binding for all three compounds. Among them, 1C exhibited the most stable profiles, with minimal variation across replicates. 2I showed slightly higher variability, including one replicate with notably weaker affinity. RAL displayed the greatest fluctuation, with one trajectory indicating exceptionally strong binding (−27 kcal mol^{-1}), while the other two remained above −13 kcal mol^{-1}. This variability likely reflects RAL's higher conformational flexibility and sensitivity to initial conditions, highlighting the influence of entropic contributions and the importance of adequate sampling.

Despite the observed inconsistencies among replicates, all ligands demonstrated an overall trend of favorable binding, in agreement with experimental data confirming their bioactivity. MM/GBSA reflects limited-timescale sampling and may underestimate slow binding dynamics or conformational reorganization. Thus, while MM/GBSA provides valuable qualitative insights into relative binding affinities, careful interpretation alongside replicate analysis and experimental correlation is essential, particularly for flexible ligands like RAL.

Per-residue decomposition of the binding free energy (enthalpic contribution only) provided insight into key protein–ligand interactions across all three complexes (Table 5). Several residues emerged as recurrent contributors, suggesting shared interaction hotspots. Notably, Leu221 was involved in stabilizing all three ligands, particularly 1C (−3.1 ± 1.3 kcal mol^{-1}) and RAL (−1.8 ± 0.7 kcal mol^{-1}), highlighting a conserved hydrophobic interaction site within the binding pocket. Similarly, Met311 appeared in both 1C and 2I complexes, consistent with its peripheral role in mediating van der Waals interactions.

TABLE 4 | MM/GBSA-derived binding free energy components for the three protein–ligand complexes.[a]

Complex	$\Delta G_{bind,w/oT\Delta S}$	$T\Delta S$	ΔG_{bind}
hTS:1C	−30.7 ± 7.2	−21.4 ± 1.6	−9.3 ± 5.9
hTS:2I	−29.9 ± 4.9	−21.4 ± 1.3	−8.6 ± 5.6
hTS:RAL	−39.8 ± 12.9	−24.2 ± 2.2	−15.6 ± 12.1

[a]Values represent the average over three independent MD simulations and include the binding free energy without entropy contribution ($\Delta G_{bind,w/oT\Delta S}$), the entropic term ($T\Delta S$), and the total binding free energy (ΔG_{bind}), all in kcal mol^{-1}.

Differences in residue contributions reflect ligand-specific binding modes. The 1C complex exhibited the most distributed and moderate interaction profile, involving multiple hydrophobic residues such as Phe225, Phe80, and Ile108, in line with its stable and moderate total binding affinity observed in MM/GBSA analysis. In contrast, RAL binding was dominated by a strong contribution from Cys195 (−7.3 ± 5.0 kcal mol^{-1}), suggesting a key polar or possibly covalent-like interaction, which may explain the large enthalpic contribution and greater variability seen in full binding energy calculations. The presence of Arg50 and Tyr258 in RAL's profile also points to a more electrostatically driven and directional binding, in contrast to the primarily hydrophobic profile of 1C.

The 2I complex showed a mixed interaction profile, with contributions from both hydrophobic (Phe117, Leu221) and polar residues (Cys195, Trp109), supporting the intermediate stability and variability seen in triplicate MM/GBSA results. Collectively, these findings suggest that while all three ligands bind within a partially overlapping site, their binding relies on distinct interaction types—ranging from hydrophobic packing in 1C to more polar or possibly flexible contacts in RAL—accounting for differences in binding strength and reproducibility across simulations.

5.6 | Analysis of Physicochemical, Biochemical, Structural, and Toxicological Characteristics (ADME) of Potent Compounds (1c & 2i)

Compounds 1c and 2i were demonstrated to have favorable ADME profiles, supporting their potential as drug-like candidates. Compound 1c, with a lower molecular weight and slightly higher lipophilicity, showed strong intestinal permeability and better predicted blood–brain barrier penetration compared to 2i. Both compounds exhibited high Caco-2 and MDCK cell permeability, indicating good oral absorption and cellular uptake. Despite 2i having a larger polar surface area, both compounds were within acceptable ranges for oral bioavailability. They also shared similar serum protein binding and had a low risk of cardiotoxicity based on hERG channel inhibition predictions. Overall, compound 1c appeared slightly more optimized in terms of drug-likeness and permeability characteristics, while compound 2i remained a viable candidate with comparable biochemical and toxicological safety (Table 6).

TABLE 5 | Contributions of key amino acid residues to the binding of C1C, C2I, and RAL to human thymidylate synthase. All values are reported in kcal mol^{-1}.

hTS:1C		hTS:2I		hTS:RAL	
Residue	ΔG_{bind}	**Residue**	ΔG_{bind}	**Residue**	ΔG_{bind}
Leu221	−3.1 ± 1.3	Cys195	−2.2 ± 1.9	Cys195	−7.3 ± 5.0
Phe225	−2.3 ± 1.0	Phe117	−1.5 ± 1.0	Ile108	−2.1 ± 0.7
Phe80	−2.1 ± 1.4	Met311	−1.0 ± 0.8	Arg50	−2.0 ± 1.3
Ile108	−1.3 ± 0.6	Leu221	−1.0 ± 1.0	Leu221	−1.8 ± 0.7
Met311	−1.0 ± 0.7	Trp109	−0.8 ± 0.7	Tyr258	−1.4 ± 1.2

17470285, 2026, 1, Downloaded from https://onlinelibrary.wiley.com/doi/10.1111/cbdd.70240 by University Of Notre Dame, Wiley Online Library on [29/10/2026]. See the Terms and Conditions (https://onlinelibrary.wiley.com/terms-and-conditions) on Wiley Online Library for rules of use; OA articles are governed by the applicable Creative Commons License

TABLE 6 | ADME characteristics of compounds **1c** and **2i**.[a]

Compound	MW	Donor HB	Acceptor HB	QPlogP o/w	QPP Caco	QPlogBB	QPlogK hsa	QPlogKp	PSA	QPlogHERG	QPPMDCK
1c	424.46	3	5.16	2.4	218.6	−0.73	1.3	−1.24	91.6	−7.3	107.601
2i	491.37	2	5.02	2.13	251.1	−1.13	1.3	−1.58	111.2	−7.5	112.106

[a]Acceptable parameters for ADME are provided in Supporting Information.

6 | Conclusion

Herein, we have reported a scalable and cost-effective synthetic route for the preparation of benzylated pyrrole-based and alkylated pyrido[2,3-d]pyrimidines. These compounds were evaluated for their anticancer potential against various cancer cell lines, including colorectal, lung, and breast cancers, as well as for their inhibitory activity against TS.

Among the synthesized compounds, 1c and 2i exhibited potent TS inhibitory activity with IC_{50} values 11.50 ± 1.08 and 17.12 ± 0.91 nM, respectively, compared to the standard inhibitor raltitrexed ($IC_{50} = 12.51 \pm 0.91$ nM). Both compounds also complied with Lipinski's rule of five, suggesting favorable drug-like properties and good oral bioavailability. In anticancer assays, compounds 1c and 2i demonstrated excellent cytotoxic activity with IC_{50} values 1.10 ± 0.61, 3.06 ± 1.25, 2.25 ± 1.73, and 4.01 ± 0.05 μM, and 1.91 ± 1.55, 3.12 ± 1.59, 4.48 ± 1.95, and 5.32 ± 1.06 μM, respectively, across the HCT 116, A549, MCF-7, and MDA-MB-231 cell lines, in comparison to raltitrexed ($IC_{50} = 1.29 \pm 0.84$, 2.27 ± 1.02, 2.98 ± 0.07, and 4.17 ± 0.72 μM, respectively).

Molecular docking studies revealed that compounds 1c and 2i displayed stronger binding affinities than raltitrexed, with key interactions at the catalytic residue Cys195 of the TS enzyme. Furthermore, compounds 1c and 2i exhibited good structural stability in molecular dynamics simulations over a 300 ns period. Based on these findings, compounds 1c and 2i emerged as promising TS inhibitors.

Acknowledgments

The authors are thankful to the CIL-Central University of Punjab, DST SERB (CRG/2023/001580) and DST-FIST for providing infrastructural support for the completion of this study. J.N. acknowledges the Croatian Science Foundation (grant IP-2022-4658), and the University of Zagreb, University Computing Center—SRCE, for granting access to the Supek supercomputer. S.R. thanks Bayer Pharmaceuticals (Application ID: PHD-2023-10682) for providing the Medha fellowship to pursue his PhD work.

Funding

This work was supported by Bayer Fellowship Program - MEDHA, Application ID: PHD-2023-10682.

Ethics Statement

The authors have nothing to report.

Consent

The authors have nothing to report.

Conflicts of Interest

The authors declare no conflicts of interest.

Data Availability Statement

Data is provided within the manuscript or Supporting Information files. The Amber trajectories of TS:ligand complexes are openly available in the FULIR repository at https://urn.nsk.hr/urn:nbn:hr:241:767449 (accessed on June 16, 2025).

17470285, 2026, 1, Downloaded from https://onlinelibrary.wiley.com/doi/10.1111/cbdd.70240 by University Of Notre Dame, Wiley Online Library on [29/10/2026]. See the Terms and Conditions (https://onlinelibrary.wiley.com/terms-and-conditions) on Wiley Online Library for rules of use; OA articles are governed by the applicable Creative Commons License

References

Alam, M. M., A. S. Almalki, T. Neamatallah, N. M. Ali, A. M. Malebari, and S. Nazreen. 2020. "Synthesis of New 1, 3, 4-Oxadiazole-Incorporated 1, 2, 3-Triazole Moieties as Potential Anticancer Agents Targeting Thymidylate Synthase and Their Docking Studies." *Pharmaceuticals* 13, no. 11: 390.

Andersen, H. C. 1983. "Rattle: A "Velocity" Version of the Shake Algorithm for Molecular Dynamics Calculations." *Journal of Computational Physics* 52, no. 1: 24–34.

Arnold, M., M. S. Sierra, M. Laversanne, I. Soerjomataram, A. Jemal, and F. Bray. 2017. "Global Patterns and Trends in Colorectal Cancer Incidence and Mortality." *Gut* 66, no. 4: 683–691.

Barrowcliff, M., and F. H. Carr. 1921. *Organic Medicinal Chemicals (Synthetic and Natural)*. Baillière, Tindall and Cox.

Besler, B. H., K. M. Merz Jr., and P. A. Kollman. 1990. "Atomic Charges Derived From Semiempirical Methods." *Journal of Computational Chemistry* 11, no. 4: 431–439.

Bisht Gunjan, S. K. A., K. Adarsh, and K. Pradeep. 2022. "A Mechanistic Study of the Antibacterial Activity of Phytoconstituents of *Pyracantha crenulata* by Using Molecular Docking Studies." *Current Chinese Chemistry* 2: e220722206994.

Case, D. A., H. M. Aktulga, K. Belfon, I. Y. Ben-Shalom, J. T. Berryman, and S. R. Brozell. 2023. *Amber 2023*. University of California.

Darden, T., D. York, and L. Pedersen. 1993. "Particle Mesh Ewald: An N Log (N) Method for Ewald Sums in Large Systems." *Journal of Computational Physics* 98: 10089.

Davisson, V., W. Sirawaraporn, and D. V. Santi. 1989. "Expression of Human Thymidylate Synthase in *Escherichia coli*." *Journal of Biological Chemistry* 264: 9145–9148.

Deep, A., P. Kumar, B. Narasimhan, et al. 2016. "2-Azetidinone Derivatives: Synthesis, Antimicrobial, Anticancer Evaluation and QSAR Studies." *Acta Poloniae Pharmaceutica* 73, no. 1: 65–78.

Dhiman, M., M. P. Zago, S. Nunez, et al. 2012. "Cardiac-Oxidized Antigens Are Targets of Immune Recognition by Antibodies and Potential Molecular Determinants in Chagas Disease Pathogenesis." *PLoS One* 7, no. 1: e28449.

Dolinsky, T. J., J. E. Nielsen, J. A. McCammon, and N. A. Baker. 2004. "PDB2PQR: An Automated Pipeline for the Setup of Poisson–Boltzmann Electrostatics Calculations." *Nucleic Acids Research* 32, no. suppl_2: W665–W667.

Eberhardt, J., D. Santos-Martins, A. F. Tillack, and S. Forli. 2021. "AutoDock Vina 1.2. 0: New Docking Methods, Expanded Force Field, and Python Bindings." *Journal of Chemical Information and Modeling* 61, no. 8: 3891–3898.

Fitzmaurice, C., T. F. Akinyemiju, F. H. Al Lami, et al. 2018. "Global, Regional, and National Cancer Incidence, Mortality, Years of Life Lost, Years Lived With Disability, and Disability-Adjusted Life-Years for 29 Cancer Groups, 1990 to 2016: A Systematic Analysis for the Global Burden of Disease Study." *JAMA Oncology* 4, no. 11: 1553–1568.

Garg, D., S. Henrich, O. M. Salo-Ahen, H. Myllykallio, M. P. Costi, and R. C. Wade. 2010. "Novel Approaches for Targeting Thymidylate Synthase to Overcome the Resistance and Toxicity of Anticancer Drugs." *Journal of Medicinal Chemistry* 53, no. 18: 6539–6549.

Genheden, S., and U. Ryde. 2015. "The MM/PBSA and MM/GBSA Methods to Estimate Ligand-Binding Affinities." *Expert Opinion on Drug Discovery* 10, no. 5: 449–461.

Gonen, N., and Y. G. Assaraf. 2012. "Antifolates in Cancer Therapy: Structure, Activity and Mechanisms of Drug Resistance." *Drug Resistance Updates* 15, no. 4: 183–210.

Hou, T., J. Wang, Y. Li, and W. Wang. 2011. "Assessing the Performance of the MM/PBSA and MM/GBSA Methods. 1. The Accuracy of Binding Free Energy Calculations Based on Molecular Dynamics Simulations." *Journal of Chemical Information and Modeling* 51, no. 1: 69–82.

Kuday, H., F. Sonmez, C. Bilen, E. Yavuz, N. Gençer, and M. Kucukislamoglu. 2014. "Synthesis and In Vitro Inhibition Effect of New Pyrido [2, 3-d] Pyrimidine Derivatives on Erythrocyte Carbonic Anhydrase I and II." *BioMed Research International* 2014: 594879.

Kumar, A., K. K. Bhagat, A. K. Singh, et al. 2023. "Medicinal Chemistry Perspective of Pyrido [2, 3-d] Pyrimidines as Anticancer Agents." *RSC Advances* 13, no. 10: 6872–6908.

Kumar, A., A. Kumar Singh, H. Singh, B. Narasimhan, and P. Kumar. 2024. "Synthesis and Anticancer Evaluation of Benzylated Indole Based Alkyl-Substituted Pyrido [2, 3-d] Pyrimidines Targeting Thymidylate Synthase." *ChemistrySelect* 9, no. 15: e202400249.

Kumar, A., J. Novak, A. K. Singh, et al. 2023. "Virtual Screening, Structure Based Pharmacophore Mapping, and Molecular Simulation Studies of Pyrido [2, 3-d] Pyrimidines as Selective Thymidylate Synthase Inhibitors." *Journal of Biomolecular Structure and Dynamics* 41, no. 23: 14197–14211.

Kumar, A., A. K. Singh, H. Singh, et al. 2025. "Synthesis and Anticancer Evaluation of Novel Pyrrole-Pyrido [2, 3-d] Pyrimidine-Based Compounds as Thymidylate Synthase Inhibitors." *Journal of Molecular Structure* 1336: 142053.

Kumar, A., A. K. Singh, H. Singh, S. Thareja, and P. Kumar. 2022. "Regulation of Thymidylate Synthase: An Approach to Overcome 5-FU Resistance in Colorectal Cancer." *Medical Oncology* 40, no. 1: 3.

Kumar, A., A. K. Singh, H. Singh, et al. 2023. "Nitrogen Containing Heterocycles as Anticancer Agents: A Medicinal Chemistry Perspective." *Pharmaceuticals* 16, no. 2: 299.

Kumar, M., G. Joshi, S. Arora, et al. 2021. "Design and Synthesis of Non-Covalent Imidazo [1, 2-a] Quinoxaline-Based Inhibitors of EGFR and Their Anti-Cancer Assessment." *Molecules* 26, no. 5: 1490.

Kumar, R., A. Kumar, A. Singh, and P. Kumar. 2023. "Design, Synthesis and Molecular Docking Studies Pyrazoline Derivatives as PI3K Inhibitors." *Combinatorial Chemistry & High Throughput Screening* 27, no. 2: 256–272.

Machado, M. R., and S. Pantano. 2020. "Split the Charge Difference in Two! A Rule of Thumb for Adding Proper Amounts of Ions in MD Simulations." *Journal of Chemical Theory and Computation* 16, no. 3: 1367–1372.

Meng, E. C., T. D. Goddard, E. F. Pettersen, et al. 2023. "UCSF ChimeraX: Tools for Structure Building and Analysis." *Protein Science* 32, no. 11: e4792.

Narella, S. G., M. G. Shaik, A. Mohammed, M. Alvala, A. Angeli, and C. T. Supuran. 2019. "Synthesis and Biological Evaluation of Coumarin-1, 3, 4-Oxadiazole Hybrids as Selective Carbonic Anhydrase IX and XII Inhibitors." *Bioorganic Chemistry* 87: 765–772.

Onufriev, A. V., and S. Izadi. 2018. "Water Models for Biomolecular Simulations." *Wiley Interdisciplinary Reviews: Computational Molecular Science* 8, no. 2: e1347.

Phan, J., S. Koli, W. Minor, R. B. Dunlap, S. H. Berger, and L. Lebioda. 2001. "Human Thymidylate Synthase Is in the Closed Conformation When Complexed With dUMP and Raltitrexed, an Antifolate Drug." *Biochemistry* 40, no. 7: 1897–1902.

Raj, A., A. Kumar, A. K. Singh, H. Singh, S. Thareja, and P. Kumar. 2023. "Synthetic Methodologies and SAR of Quinazoline Derivatives as PI3K Inhibitors." *Anti-Cancer Agents in Medicinal Chemistry* 23, no. 9: 1013–1047.

Roe, D. R., and T. E. Cheatham III. 2013. "PTRAJ and CPPTRAJ: Software for Processing and Analysis of Molecular Dynamics Trajectory Data." *Journal of Chemical Theory and Computation* 9, no. 7: 3084–3095.

Sarkar, B., M. Dhiman, S. Mittal, and A. K. Mantha. 2017. "Curcumin Revitalizes Amyloid Beta (25–35)-Induced and Organophosphate

17470285, 2026, 1, Downloaded from https://onlinelibrary.wiley.com/doi/10.1111/cbdd.70240 by University Of Notre Dame, Wiley Online Library on [29/10/2026]. See the Terms and Conditions (https://onlinelibrary.wiley.com/terms-and-conditions) on Wiley Online Library for rules of use; OA articles are governed by the applicable Creative Commons License

Pesticides Pestered Neurotoxicity in SH-SY5Y and IMR-32 Cells via Activation of APE1 and Nrf2." *Metabolic Brain Disease* 32: 2045–2061.

Shih, C., V. J. Chen, L. S. Gossett, et al. 1997. "LY231514, a Pyrrolo [2, 3-d] Pyrimidine-Based Antifolate That Inhibits Multiple Folate-Requiring Enzymes." *Cancer Research* 57, no. 6: 1116–1123.

Sung, H., J. Ferlay, R. L. Siegel, et al. 2021. "Global Cancer Statistics 2020: GLOBOCAN Estimates of Incidence and Mortality Worldwide for 36 Cancers in 185 Countries." *CA: a Cancer Journal for Clinicians* 71, no. 3: 209–249.

Taddia, L., D. D'Arca, S. Ferrari, et al. 2015. "Inside the Biochemical Pathways of Thymidylate Synthase Perturbed by Anticancer Drugs: Novel Strategies to Overcome Cancer Chemoresistance." *Drug Resistance Updates* 23: 20–54.

Tian, C., K. Kasavajhala, K. A. Belfon, et al. 2019. "ff19SB: Amino-Acid-Specific Protein Backbone Parameters Trained Against Quantum Mechanics Energy Surfaces in Solution." *Journal of Chemical Theory and Computation* 16, no. 1: 528–552.

Tosco, P., N. Stiefl, and G. Landrum. 2014. "Bringing the MMFF Force Field to the RDKit: Implementation and Validation." *Journal of Cheminformatics* 6: 1–4.

Wahba, A. J., and M. Friedkin. 1962. "The Enzymatic Synthesis of Thymidylate: I. Early Steps in the Purification of Thymidylate Synthetase of *Escherichia coli*." *Journal of Biological Chemistry* 237: 3794–3801.

Wang, J., W. Wang, P. A. Kollman, and D. A. Case. 2006. "Automatic Atom Type and Bond Type Perception in Molecular Mechanical Calculations." *Journal of Molecular Graphics & Modelling* 25, no. 2: 247–260.

Wang, J., R. M. Wolf, J. W. Caldwell, P. A. Kollman, and D. A. Case. 2004. "Development and Testing of a General Amber Force Field." *Journal of Computational Chemistry* 25, no. 9: 1157–1174.

Ward, W. H., R. Kimbell, and A. L. Jackman. 1992. "Kinetic Characteristics of ICI D1694: A Quinazoline Antifolate Which Inhibits Thymidylate Synthase." *Biochemical Pharmacology* 43, no. 9: 2029–2031.

Supporting Information

Additional supporting information can be found online in the Supporting Information section. **Appendix S1:** Supporting Information.

17470285, 2026, 1, Downloaded from https://onlinelibrary.wiley.com/doi/10.1111/cbdd.70240 by University Of Notre Dame, Wiley Online Library on [29/10/2026]. See the Terms and Conditions (https://onlinelibrary.wiley.com/terms-and-conditions) on Wiley Online Library for rules of use; OA articles are governed by the applicable Creative Commons License